LUNDS UNIVERSITET

Diode laser spectroscopy for oxygen detection in the lungs of infants

Author:

Peilang Liao

Supervisor:

Patrik Lundin

Co-supervisor:

Stefan Andersson-Engels

Jim Larsson

This is a thesis submitted for the degree of Master of Science Project. The aim is to construct both a simulation based and a physical model of the torso of a small infant, to evaluate the optical properties. The application of these studies is for a larger project where the oxygen concentration in the lungs should be measured using laser spectroscopy.

Project duration: Oct, 2015 to May, 2016

Bio Photonics

Atomic Physics

Department of Physics, Lund University

Contents

1 Abstract **6**

2 Introduction **7**
2.1 Optical properties of biological tissues 7
2.1.1 Absorption 7
2.1.2 Scattering 8
2.2 Mathematical model of light propagation 8
2.3 Inverse solution of light propagation 9
2.4 Brief description of tissues and their optical properties 10
2.4.1 Computed tomography image 10
2.4.2 Skin 11
2.4.3 Fat tissue 12
2.4.4 Muscle 12
2.4.5 Heart 12
2.4.6 Lung 13
2.4.7 Bone 13
2.5 Summary of optical properties of interesting organs 14
2.6 Conclusion of optical properties to be used 17
2.7 GASMAS theory 18
2.7.1 Tunable Diode Laser Absorption Spectroscopy (TDLAS) 18
2.7.2 Wavelength modulation spectroscopy 18
2.7.3 GAs in Scattering Media Absorption Spectroscopy (GASMAS) . 20
2.7.4 Signal processing 21
2.7.5 Optical interference 22
2.7.6 Signal calibration from reference arm 23
2.7.7 Equivalent path length from water vapour detection 24
2.8 DICOM image 25
2.9 Modeling Near-Infrared light transport in tissue 25

3 Methodology **26**
3.1 Simulation Work 26
3.1.1 CT image segmentation with Nirfast 26
3.1.2 Detection geometry evaluation 29
3.2 Computer file for 3D phantom printing 30
3.3 Preparation of liquid phantom 31
3.4 Experiment with GASMAS system 32
3.4.1 Sample arm measurement 33
3.4.2 Nitrogen flushing measurements 34
3.4.3 Reference measurement 35

4 Result **36**
4.1 3D printed model 36
4.2 Liquid phantom optical properties 36
4.3 Nirfast simulation 36
4.4 GASMAS measurement 41
4.4.1 Reference measurements 41
4.4.2 Sample measurements 41
4.4.3 Nitrogen vs air 45

5 Summary and Outlook **48**

6 Appendix.A - Printed tissue models **54**

7 Appendix.B - calculation of predicted optical properties at correct wavelengths from literature **56**

8 Appendix.C - WMS signal phase adjusting and intensity normalisation **59**

Abbreviation

CT ..... Computed Tomography

RDS ..... Respiratory Distress Syndrome

NIR ..... Near Infra-Red

PTOF ..... Photon Time-of-Flight

TCSPC ..... Time Corrected Single Photon Counting

PMT ..... Photon Multiplier Tube

CFD ..... Constant Fraction Discriminator

TAC ..... Time to Amplitude Converter

SIS ..... Single Integrating Sphere

TDLAS ..... Tunable Diode Laser Absorption Spectroscopy

GASMAS .... GAs in Scattering Media Absorption Spectroscopy

WMS ..... Wavelength modulation spectroscopy

SNR ..... Signal To Noise Ratio

FWHM ..... Full Width at Half Maximum

APD ..... Avalanche Photo Diode

DICOM ..... Digital Imaging and Communication in Medicine

Acknowledgement

I would first like to thank my thesis advisor Stefan Andersson-Engels, the professor in atomic physic of the science faculty at Lund university. I am very appreciated that he offered me such a great project. Whenever I ran into trouble or had questions, the door to Prof. Stefan was always opened. The inspiration, advice and encourage from him drove me to accomplish the project confidently.

Also I would like to thank my main supervisor, Patrik Lundin from Gasporox AB in Lund, and Jim Larsson, the PhD from combustion physics department of the science faculty. With their passionate participation and input, in the lab experiment or in the thesis writing, the progress of the thesis could not have been successfully conducted.

I would also like to thank the experts who kindly offered help to me whenever I have doubts, and my classmates Lisa, Hasti and Alex, with whom we spent a wonderful time together in fighting the thesis work.

Finally, I would like to thank my family for providing me with unfailing support. They never feel disappointed at me, but instead, giving me continuous encouragement throughout my years of study. The accomplishment would not have been possible without them. Thank you.

1 Abstract

This thesis work is part of a larger project with final goal to be able to measure the oxygen concentration in the lungs of infants, using non-invasive laser spectroscopy. This thesis is specifically dealing with simulations of light transport through the upper body of infants, as well as constructing a tissue-like model (phantom) that can be used in experiments. The goal is to use these simulations, along with measurements on the phantoms to obtain a better knowledge about how the final measurement system should be designed. The phantoms are constructed to have similar structures to an infant and correct optical properties. The gas detection in the lung of the phantom is implemented by GASMAS, which stands for GAs in Scattering Media Absorption Spectroscopy. It utilises a laser at 760 nm for oxygen detection and a laser at 935 nm for water vapour detection. The software employed to do numerical simulations is named Nirfast. It includes two parts, one is to do segmentation of different tissues from a series of CT images, and based on that, light propagation simulations are done; the other one is to do measurement geometry evaluation, in which we define a parameter of sensitivity to indicate how a measurement geometry is sensitive to the gas in the lung. The measurement geometries that have a high sensitivity value are selected and are used for GASMAS measurements. An extensive literature research on optical properties at 760 nm of skin, fat, muscle, lung, heart and bone (the segmented tissues) is done and the values are applied to the simulation. There are two kinds of phantoms, one is the 3D printed models of only the boundary of different tissues. The other one is the liquid phantom of fat, muscle and heart with correct μ_a and μ_s', made of Indian ink and intralipid. GASMAS measurements on both water vapour and oxygen are done at atmospheric conditions (21% oxygen) and the results are compared to the simulation results.

2 Introduction

Currently, a relatively large part of the preterm infants suffer from a common lung disease called Respiratory Distress Syndrome (RDS). It is caused by insufficiency of the surfactant (alveoli coating protein) in their immature lungs. As a complement for X-ray detection, the oxygen detection in the lungs is an alternative way to investigate the severity of such a disease. Thus we introduce GASMAS, GAs in Scattering Media Absorption Spectroscopy, a non-invasive laser diagnostic technique for gas detection. From previous clinical trial experience [1], the detection was done by moving the probe and detector 'randomly' around the body until a rather good absorption signal was detected, however, this acquired a lot of effort at the clinic. Besides, the signal is normally weak and the accuracy of detected oxygen concentration is not guaranteed. So for the overall goal of this project, we want to evaluate the probe-detection measurement geometry in order to better understand which regions are preferable for a precise oxygen detection, and how to process the measurements. This is mainly done by simulating light propagation in a digital model whose optical properties mimic an infant. A robust and physical phantom based on the digital model is then constructed to implement GASMAS oxygen measurements, as a reference to examine the validity of the simulation results. Both the simulation and the 3D model construction are new attempts which have not been done before, and it could be of great interest and of valuable help for system design. This thesis project is a part of the early stages of an EU project running right now, and the thesis will contribute to designing of the system.

2.1 Optical properties of biological tissues

2.1.1 Absorption

Two main phenomena contribute to the light attenuation in a scattering medium: absorption and scattering. In biological tissues, the absorption originates from the light absorption of chromophores, for example, melanin absorbs a certain amount of light intensity, depending on the wavelength of incident light. It is commonly assumed that four main chromophores in tissues, namely water [2], fat (lipids) [3], oxygenated and deoxygenated hemoglobin (blood), with their associated concentrations, can be sufficient enough to describe absorption. This is then described as the absorption coefficient, $\mu_a(\lambda)$, cm^{-1}. See equation (1):

$$\mu_a(\lambda) = B \cdot Sat \cdot \mu_{a,oxy} + B \cdot (1 - Sat) \cdot \mu_{a,deoxy} + W \cdot \mu_{a,water} + IL \cdot \mu_{a,lipid} \ , \qquad (1)$$

where Sat is the oxygen saturation of blood, and B, W and IL represent the volume fraction of blood, water and intralipid, respectively. The absorption coefficient is wavelength dependent (figure 1). The red-infrared range (700 nm $\sim$ 1 mm) is thus commonly referred as the tissue diagnostic window because the overall absorption coefficient (the dashed line) is rather low in this region.
According to equation (1), the concentrations of these four chromophores can be retrieved if the values of $\mu_a(\lambda)$ at at least four different wavelengths are known.

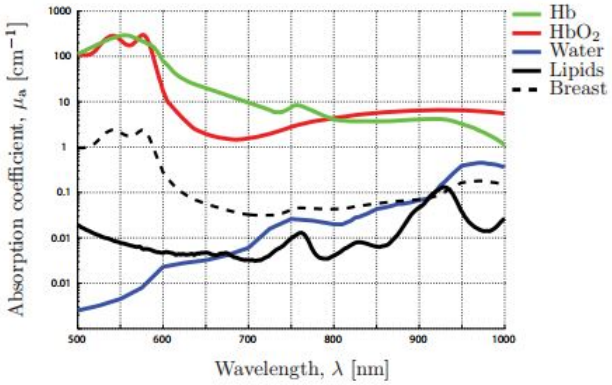

Figure 1: The absorption spectrum [4] for the four chromophores in breast tissue. The dashed line is the overall absorption given by the concentration of 50% water, 30% lipids and 20μM hemoglobin at 75% oxygenation.

2.1.2 Scattering

Scattering is due to the presence of particles and varying refractive index between interfaces in the medium. In tissue, for visible and NIR light, the scattering originates mainly from cell nuclei and sub cellular organelles at a microscopic level [5]. The scattering is affected by both the size and the density of the scatterers. According to Rayleigh and Mie scattering, the wavelength dependence of the scattering coefficient μ_s, cm^{-1}, can be expressed as:

$$\mu_s(\lambda) = a_m \cdot \frac{\lambda^{-b}}{\lambda_0} + a_R \cdot \frac{\lambda^{-4}}{\lambda_0} \ , \tag{2}$$

where λ_0 is the reference wavelength, a_m and a_R are the scattering amplitude that provides the information on the density of the scattering medium; b represents the scattering power related to the size of scattering substance and for Rayleigh scattering, b equals to $b = 4$. This expression implies that $\mu_s(\lambda)$ decreases as the wavelength increases, the spectrum of which will show no characteristic peaks but a smooth curve.

2.2 Mathematical model of light propagation

Given the assumption that the optical properties are homogeneous everywhere in a scattering medium, the most common analytical model to describe how light propagates is the transport theory [6][7]. If the scattering coefficient is much larger than the absorption coefficient, a so-called diffusion equation can be used to mathematically represent the light propagation:

$$\frac{1}{c} \cdot \frac{\delta\phi(\hat{r},t)}{\delta t} - D \cdot \bigtriangledown^2\phi(\hat{r},t) + \mu_a\phi(\hat{r},t) - S(\hat{r},t) = 0 \ , \tag{3}$$

where $c = c_0/n$ is the velocity of light in tissue, n is the refractive index; $\hat{r}$ is the separation between the source and detector; $\phi(\hat{r},t)$ in unit $[\mathrm{W/m}^2]$ is the fluence rate

(the radiance field) that we want to detect; $S(\hat{r}, t)$ is the light source term; D equals to $[3(\mu_a + \mu'_s)]^{-1}$, in which μ'_s is the reduced scattering coefficient that equals to $(1-g)\mu_s$, and $g =< cos(\theta) >$ is the mean of the cosine of the scatter angle. The reduced scattering coefficient is explained as the mean path length for a photon to completely lose its original incident direction. For the optical properties that we discuss over the whole thesis, it is the reduced scattering coefficient that is used. For different measurement geometries, we get different solutions to the fluence rate $\phi(\hat{r}, t)$ which are available from literature. For example, in the case of infinite geometry where there is no boundary condition [8] and the light source $S(\hat{r}, t)$ is a point source of $2D$ Dirac function as $\delta(0, 0)$, a solution to equation (3) is given by:

$$\phi(\hat{r}, t) = c \cdot (4\pi D \cdot ct)^{-3/2} \cdot exp(-\frac{r^2}{4Dct} - \mu_a \cdot ct) \ . \tag{4}$$

2.3 Inverse solution of light propagation

There are two basic approaches in studying the light propagation:

- Forward solution: estimation of the fluence rate according to the diffusion equation (3) with known optical properties.
- Inverse solution: extraction of the optical properties by measuring the fluence rate.

One of the most frequently used techniques to solve the inverse solution is the Photon Time-of-Flight (PTOF) measurement [9] (figure 2). This is a time-domain measurement where a short light pulse ($\sim$ 100 ps duration) is injected into a scattering medium. At a certain distance from the injection point, the distribution of photon time-of-flights is detected, allowing to gather information of optical properties of this medium. However, commonly a detector has a few nanoseconds of dead time during which another photon event can not be registered after the first photon event is received. To avoid the dead time, the Time Corrected Single Photon Counting (TCSPC) system is employed where the light intensity is attenuated until only one or zero photons will reach the detector during a pulse period [10]. Another arm (indicated by SYNC in figure 2), which is also attenuated, is synchronized to the sample arm. The measured time delay of photon between these two arms makes up the photon time-of-flights distribution.

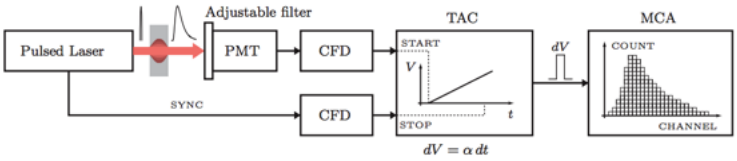

Figure 2: A pulsed laser is split into the sample arm and reference arm; when a single photon arrives to the Photon Multiplier Tube (PMT), it triggers an electric pulse and the pulse is amplified; the signal is then sent to a Constant Fraction Discriminator (CFD), which is used to improve the timing of the generated electric pulse; a clock starts whenever the reference pulse is registered and the clock stops when the signal is detected; the time delay between these two arms is then sent to a Time to Amplitude Converter (TAC), and is converted to an electric voltage; a histogram of time-of-flights distribution is built up.

The injected laser pulse will experience attenuation and pulse shape broadening because of the scattering and the absorption in the sample. Absorption mainly determines how steep the temporal tail is at longer times of the broadened pulse. The longer times the photons stays in the tissue, the higher is the probability to be absorbed (figure 3a). Scattering mainly specifies the broadening of the pulse because it determines the time for photons to reach the detector. See figure 3b.

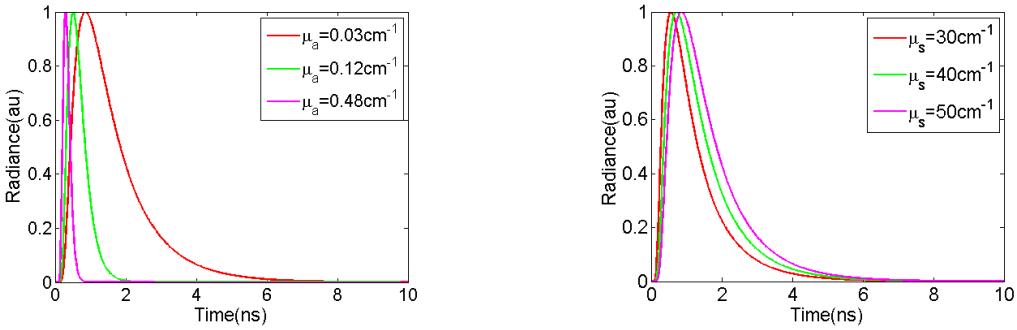

Figure 3: a) The tail of the pulse is changed when μ_a is changed only. b) The broadening is altered when μ_s' is changed only.

One way to extract the optical properties from a tissue is to numerically fit the theoretical expression of the fluence rate to the experimental photon distribution. This is proceeded by changing the variable μ_a and μ_s' until it reaches a certain error tolerance.

2.4 Brief description of tissues and their optical properties

2.4.1 Computed tomography image

Computed Tomography (CT) is an imaging technique that scans a patient with X-ray radiation in a large number of directions. This results in a series of gray scale images

where different tissues appear in different intensity. For example, bone appears white in a CT image because calcium has a much higher absorption of X-ray than lung tissue mostly filled of air that does not attenuate X-ray. Thus, the lung appears black in a CT image. Figure 4 shows a slice CT image of a 3.8 kg infant.

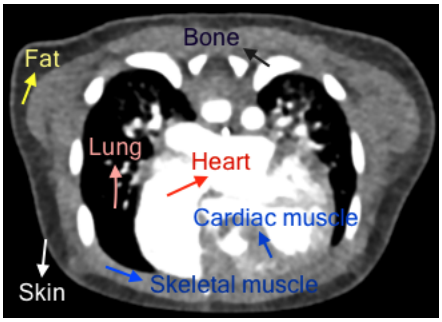

Figure 4: Six different tissue types: skin, fat, skeletal muscle and cardiac muscle, lung, heart and bone, indicated by arrows and texts, are shown in this CT image.

2.4.2 Skin

Skin is the very outside tissue that protects inner organs and tissues from physical, mechanical, chemical and pathogenic microorganisms' invasion. Skin demonstrates highly heterogeneous properties due to the complex structure of varied distributed blood vessel, lymph, nerve, sweat gland and so on. The thickness of skin differs from human to human and from part to part of the body. Literately skin consists of three layers, namely epidermis, dermis and subcutaneous tissue. Epidermis, which has a thickness typically around $100 - 150$ μm, is a blood-free layer and mostly contains skin pigment, especially melanin [11]. Dermis with a thickness typically around $1 - 4$ mm is the vascularized layer where there is an abundance of blood vessels. Thus we could say that for the whole skin, the absorption properties are defined by lipids in skin epidermis and the hemoglobin and water in skin dermis [11]. Figure 5a shows absorption coefficient spectrum of the skin simulated according to equation (1), presented under at three different conditions of blood.

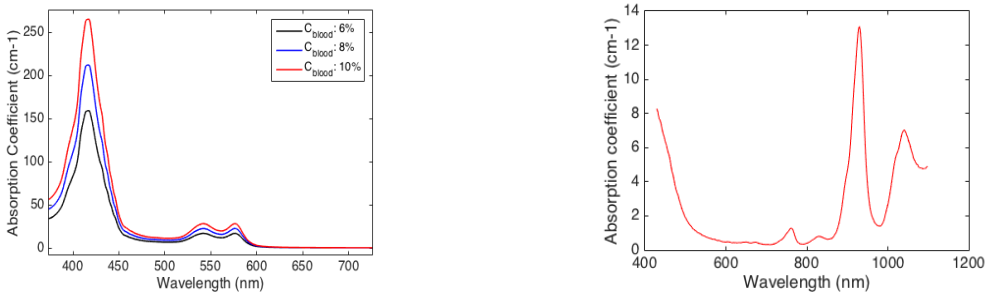

(a) (b)

Figure 5: a) The μ_a spectrum of the skin at three different blood concentrations of 6%, 8% and 10%, all at oxygen saturation of 80%, given the lipid concentration of 30%, 28% and 26%, respectively, and all three cases with water concentration of 64%. b) The spectrum of fat absorption coefficient, the value of which is averaged between the measurements performed at 37°C and 60°C.

2.4.3 Fat tissue

As mentioned above, the layer beneath the top two layers of epidermis and dermis is the subcutaneous tissue, or also called the inner fat layer in general. The fat contained in the subcutaneous tissue layer is referred to adipose tissue which contains mostly the aggregation of fat cells that contains the lipid in the form of small droplets. The subcutaneous tissue has a thickness of a few millimeters, depending on individual. The absorption properties of subcutaneous tissue is defined by hemoglobin, water and lipid, where lipid accounts for most of the concentration. A spectrum of the absorption coefficient versus wavelength is studied from a clear purified oil obtained from pig lard [3]. See figure 5b.

2.4.4 Muscle

Muscle has three types: skeletal muscle, smooth muscle and cardiac muscle. The main light absorbers in muscle are myoglobin and hemoglobin. Figure 6 shows the optical properties of muscle obtained from a data base from Biomedical Optics Research Laboratory, UCL Department of Medical Physics and Biomedical Engineering [12]. The measurement method uses diffuse reflectance and transmittance, and single integrating sphere (SIS) technique to the 1.5 to 2 mm thick samples. These muscle tissue samples are ex-vivo from either plastic surgery or post mortem examinations.

2.4.5 Heart

The heart wall that surrounds the left and right arial are cardiac muscle, which is a type of muscle tissue. Inside the heart wall there is pure blood. The blood inside the heart wall is shown as white in a CT image because its contrast is improved by

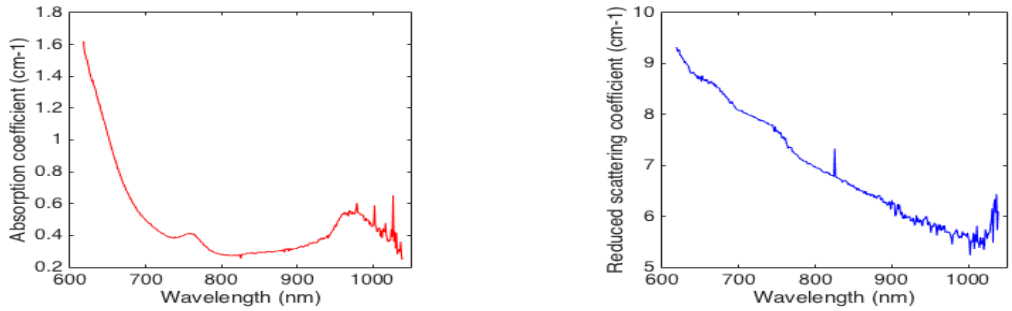

(a) (b)

Figure 6: a) The spectrum of absorption coefficient of the muscle. b) The spectrum of reduced scattering coefficient.

targeting some contrast agent to the blood, which has a higher attenuation response to X-ray than that of only the blood itself. As to the heart wall, the cardiac muscle, is assimilated as skeletal muscle because they have the same intensity range in a CT image (figure 4). Thus, the optical properties of the heart can be approximated as those of pure blood. The blood is constituted of 45% for red blood cells and 55% for plasma, out of which 90% is water. When the hematocrit (the percentage of blood that is cell) and the quantity of hemoglobin in each cell are in the normal situation, the red blood cell contains 16 grams of hemoglobin per deciliter for men, and 14 grams per deciliter for women [13]. The density of hemoglobin, 1060 kg/m^3 [14], is almost the same as water which is 1000 kg/m^3 , so we can say about 14% out of the red blood cell is hemoglobin. Generally speaking, the hemoglobin in body is around $14\% \times 45\% = 6.3\%$ with oxygen saturation about 80%.

2.4.6 Lung

The lungs are a pair of spongy organs that are almost air-filled, sitting on either side of the chest. When we breath, the air first goes through the trachea, which is then divided into two primary bronchi, then further divided into smaller structure of bronchioles, eventually ended up in clusters of tiny air sacs called alveoli, surrounded by blood vessels. The alveoli is where the oxygen and the carbon dioxide are exchanged from, or into, the blood. Although the lung is so called air-filled, the 'tree structure' of bronchioles gives the lung extremely heterogeneous properties. In our study, this kind of physiological structure is complex to simulate, instead a complete void is considered.

2.4.7 Bone

Bone consists of cortical bone (the hard outer layer and accounts for 80% of the total bone mass), cancellous bone (filling the interior of the bone), and bone marrow (blood vessels and nerve inside). However, the bone composition or chromophore components ratio vary a lot from age to age, and so far there is no measurement on bones of infants.

Thus, it is not possible to obtain the optical properties of neonatal bone from literature, instead, the properties of adult bone need to be used.

2.5 Summary of optical properties of interesting organs

Table 1 shows the summary of literature data of the optical properties of the six tissues mentioned above:

Table 1: Optical Properties found from literature

Tissue	Wavelength,nm	μ_a,cm^{-1}	μ_s',cm^{-1}	Measurement Method	Sample information	Reference
Skin	700 800 900 1000	0.48(0.11)[1] 0.43(0.11) 0.33(0.02) 0.27(0.03)	16.7(2.3) 14.0(1.9) 15.7(2.1) 16.8(2.8)	measure is performed in Vitro and Ex Vivo; IS,IAD[2]	caucasian skin with n=21,whole skin, 1 $\sim$ 6 mm, postmortem, 24hr after death, stored at 20°C in saline, measurement at room temp. $\mu_s' = 1.1 \times 10^{12}\lambda^{-4} + 73.7\lambda^{-0.22}$, [$\lambda$] in nm	[11]
Fat	700 800 900 1000	1.11(0.05) 1.07(0.11) 1.07(0.07) 1.06(0.06)	12.2(4.4) 11.6(4.6) 10.0(3.4) 9.39(3.3)	measure is performed in Vitro and Ex Vivo; IS, IAD	Human subcutaneous adipose tissue (n = 6); Tissue slabs, 1 $\sim$ 3mm; 6 h after surgery; Stored at 20°C in saline; measurements at room temperature.$\mu_s' = 1.05 \times 10^3\lambda^{-0.68}$, [$\lambda$] in nm	[11]
Muscle	700 750 800 850 900 950	0.48 0.41 0.28 0.3 0.32 0.46	8.18 7.71 7.04 6.67 6.21 5.9	measure is performed in Vitro;IS,IMC	$n = 1$, samples from abdominal and breast tissue obtained from plastic surgery or postmortem examination. $\mu_s' = 7.67 \times 10^3\lambda^{-1.045}$, [$\lambda$] in nm	[11]
Lung	632.8 790 850	2.0(0.1) 2.4(0.3) 0.76(0.07)	19.7(1.4) 20.0(1.7) 10.9(0.7)	measurement in vitro and ex vivo	a piglet	[11]
Heart	532 660 745	8.9 0.7 0.5	148 118 108	Measurement in ex vivo with PTOF technique	It is the measured optical properties of myocardium (not really the heart). At all wavelength, the g factor is 0.95 and refractive index is n = 1.4for theses healthy myocardium	[15]
Aorta	753.8 764.1 755.6 767.3 756.9 765.7	2.33 2.246 1.739 1.675 4.005 3.854	161 169 275.6 270.2 202.94 199.9	Measurement in ex vivo with IS and collimated transmission	These samples were obtained within 24h of death and were stored at 20°C before measurement.	[16],intima [3] [16],medium [16],adventitia
Skull	760 820 935	0.21 0.21 0.33	9.5 9.1 8.5	Measurement in Vitro with PTOF techinique	A summary from different human skull samples, measured by different research groups	[17]

[1]The value in parentheses is rms.

[2]The technique used to measure the optical properties: IS represents Integrating Sphere Technique, IAD is the Inverse Adding-Doubling Technique, and IMC is the Inverse Monte Carlo.

[3]The intitia is the thin endothelial lining inside the aorta; the medium is the thick layer consisting of muscle cell, collagen and elastin; the adventitia is the outside coating layer, mainly fibres.

As we have mentioned in the abstract, only the optical properties of these tissue obtained at wavelength of 760 nm is of main interest. Three more wavelengths at 725 nm, 820 nm and 935 nm are in potential use. Table 2 lists the optical properties of skin, fat and muscle at these correct wavelengths. The μ_a and μ_s' are calculated assuming that we can only use water, lipid, oxygenated and de-oxygenated hemoglobin to represent the absorption coefficient and by retrieving their concentration from table 1 according to equation (1). See appendix B for calculation. Thus the absorption coefficient at any wavelength can be calculated by combining the calculated chromophore concentrations and their well-known absorption spectrum (figure 1).

Table 2: Optical properties calculated from data base

Tissue	Wavelength,nm	μ_a,cm^{-1}	μ_s',cm^{-1}	Measurement Method	Reference
Skin	725	0.376	22.021	measure is performed in computer simulation. While the μ_s' is calculated from the corresponding scattering equation in table 1	[18]
	760	0.476	19.621		
	820	0.433	18.178		
	935	0.060376	17.224		
Fat	725	0.899	11.916	measure is performed in computer simulation. While the μ_s' is calculated from the corresponding scattering equation in table 1	[18]
	760	1.180	11.540		
	820	1.102	10.959		
	935	0.560	10.024		
Muscle	725	0.3491	7.8658	measure is performed in computer simulation. While the μ_s' is calculated from the corresponding scattering equation in table 1	[18]
	760	0.4519	7.4876		
	820	0.2745	6.9161		
	935	0.3524	6.0297		

As we can see, the calculated optical properties show a coincident with the corresponding values in table 1.

A recent overview of optical properties, specified in the reduced scattering coefficient, of different tissues can be found in the review from Steve Jacques [19]. In his paper, a general expression of the reduced scattering coefficient as a function of wavelength can be described as:

$$\mu_s' = a\left(\frac{\lambda}{500\,\mathrm{nm}}\right)^{-b} \quad , \tag{5}$$

where a is the scaling term with the value equal to $\mu_s'(500nm)$, and b is the scattering power. Theoretically the scattering properties can be characterised by Mie and Rayleigh scattering. So alternatively, the equation can also be expressed as:

$$\mu_s'(\lambda) = a'\left(f_{Ray}\left(\frac{\lambda}{500\,\mathrm{nm}}\right)^{-4} + (1-f_{Ray})\left(\frac{\lambda}{500\,\mathrm{nm}}\right)^{-b_{Mie}}\right) \quad , \tag{6}$$

where a' is the scaling term with the value equal to $\mu_s'(500nm)$, b_{Mie} is the scattering power and f_{Ray} indicating the contribution from Rayleigh scattering. Table 3 is a collection from the tables in reference [19] which shows the parameters mentioned above to predict the reduced scattering coefficient. As we can see these parameters for a single

Table 3: Optical Properties found from literatures

Tissue	a,cm^{-1}	b	a',cm^{-1}	f_{Ray}	b_{Mie}	Ref.	Literature
Skin	48.9	1.548	45.6	0.22	1.184	Skin	Anderson *et al* 1982
	47.8	2.453	42.9	0.76	0.351	Skin	Jacques 1996
	37.2	1.390	42.6	0.40	0.919	Skin	Simpson *et al* 1998
	60.1	1.722	58.3	0.31	0.991	Skin	Saidi*et al* 1995
	29.7	0.705	36.4	0.48	0.220	Skin	Bashkatov*et al* 2011
	45.3	1.292	43.6	0.41	0.562	Dermis	Salomatina*et al* 2006
	68.7	1.161	66.7	0.29	0.689	Epidermi	Salomatina*et al* 2006
	30.6	1.100	na	na	na	skin	Alexandrakis*et al* 2005
Mean	46.0	1.421	48.0	0.409	0.702		
SD	13.7	0.517	10.6	0.178	0.351		
num	8	8	7	7	7		
Muscle	13.0	0.926	13.0	0.00	0.926	Muscle	Tromberg 1996
	9.8	2.820	na	na	na	Muscle	Alexandrakis *et al* 2005
Lung	25.4	0.530	na	na	na	Lung	Alexandrakis *et al* 2005
	8.1	0.980	8.1	0.00	0.980	Lung	Alexandrakis *et al* 2005
Heart	14.6	1.430	na	na	na	Heart wall	Alexandrakis *et al* 2005
	8.3	1.260	8.3	0.00	1.260	Heart	Yi and Backman 2012
Bone	9.5	0.141	9.7	0.04	0.116	Skull	Bevilacqua *et al* 1989
	20.9	0.537	20.9	0.00	0.537	Skull	Firbank *et al* 1993
	38.4	1.470	na	na	na	Bone	Alexandrakis *et al* 2005
Fatty tissue	13.7	0.385	14.7	0.16	0.250	Subcutaneous fat	Simon *et al* 1998
	10.6	0.520	11.2	0.29	0.089	Adipose breast	Peters *et al* 1990
	15.4	0.680	15.4	0.00	0.680	Subcutaneous adipose	Bashkatov *et al* 2011
	35.2	0.988	34.2	0.26	0.567	Subcutaneous fat	Salomatina *et al* 2006
	21.6	0.930	21.1	0.17	0.651	Subcutaneous adipocytes	Salomatina *et al* 2006
	14.1	0.530	na	na	na	Adipose	Alexandrakis *et al* 2005
Mean	18.4	0.672	19.3	0.174	0.447		
SD	9.0	0.242	9.1	0.111	0.263		
num	6	6	5	5	5		

Table 4: Calculated μ_s' at 760nm

Tissue	a,cm^{-1}	b	a',cm^{-1}	f_{Ray}	b_{Mie}	$\mu_s', cm^{-1}, Eq5$	$\mu_s', cm^{-1}, Eq6$
Skin(mean)	46.0	1.421	48.0	0.409	0.702	25.3722	24.8212
Muscle	13.0	0.926	13.0	0.00	0.926	8.8218	8.8218
	9.8	2.820	n	na	na	3.0090	na
Lung	25.4	0.530	na	na	na	20.3449	na
	8.1	0.980	8.1	0.00	0.980	5.3334	5.3738
Heart	14.6	1.430	na	na	na	8.0226	na
	8.3	1.260	8.3	0.00	1.260	4.8973	4.8973
Bone	9.5	0.141	9.7	0.04	0.116	8.9554	8.9432
	20.9	0.537	20.9	0.00	0.537	16.6915	16.6915
	38.4	1.470	na	na	na	20.7501	na
Fat (mean)	18.4	0.672	19.3	0.174	0.447	13.8873	13.8493

tissue type can be different according to literature. Table 4 shows the calculated μ_s' at wavelength 760 nm, by using both equation (5) and (6).

From the calculation in table 4, equation (5) and (6) have similar calculated scattering coefficient. We should notice that the calculation for skin and fat tissue use the mean value of the parameters (see the blue text in table 3) due to the large amount literature

data and rather low standard deviation of these value. For the rest tissue type, they have few data to support the reliability and values of these parameters may vary a lot for different studies. The sample used can be different from person to person, young to old and time to time, and the measurement techniques are different for different research groups. So it is not reasonable to calculate the mean optical properties for muscle, lung, heart and bone. For a preterm or full term infant, it is hard to get the relative optical properties of these kinds of tissue, and even harder to predict the scattering coefficient at the correct wavelengths.

2.6 Conclusion of optical properties to be used

So far an extensive effort has been applied to summarise the optical properties of different tissues, because we want to make liquid phantoms of lung, heart, muscle, fat and skin that have a correct μ_a and μ_s'. The bone is not considered here because it is printed solid with the material of nylon with fixed optical properties (which will be discussed in a later section). As we have mentioned before, tissue optical properties can be approximately described by only using water, lipid, oxygenated and de-oxygenated hemoglobin. Table 5 shows how the composition of these four chromophores should be in order to reasonably represent a tissue type:

Table 5: The composition of different tissues

Tissue	hemoglobin	oxygen Saturation	water	lipid	Ref.	λ,nm	μ_a, cm^{-1}
skin	6%	75%	64%	30%	[20]	760nm	0.28
fat	2%	75%	13∼ 38%	60∼ 85%	[21][22]	760nm	0.103 ∼ 0.106
Muscle	5%	60%	79%	16%	[20]	760nm	0.284
Heart(blood)	6.3%	80%	90%	0%	[14]	760nm	0.287
Lung	1∼ 8%	75%	84%	8∼ 15%	[20]	760nm	0.06 ∼ 0.379

The water content for different tissue types is well determined from current literature (reference column in the table), but it is not the case for hemoglobin and lipid. The fat tissue has a very small volume of blood because capillaries are in contact with subcutaneous tissue; the muscle has a rather high blood volume than fat tissue, but less than the heart which is considered as just pure blood. Again, the reason is that the heart wall (the cardiac muscle) is assimilated as skeletal muscle, and inside the heart wall is the blood. As a result, by comparing and weighting table 5, to table 1, 2, 3 and 4, the general optical properties of different tissues are summarised and the values would be applied during the thesis work. See table 6 and we should notice that the bone has the optical properties of nylon which is the material that used to print the 3D phantom that holds these liquid phantom.

Table 6: To be used optical properties at $760nm$

Tissue	μ_a, cm^{-1}	μ_s', cm^{-1}	From:
skin	0.35	15.7	table 2&5
Fat	0.10	10	table 5
Muscle	0.284	7.49	table 2&5
Lung	0.20	10	table 5
Heart(blood)	0.287	4.89	table 4&5
Bone	0.02	46.53	$\mu_{a,nylon}$, $\mu'_{s,nylon}$

During the experimental work, Indian ink [23][24], as the absorption origin, and Intralipid of 20% suspension [23][25], as the scattering origin, are used to make the liquid phantoms.

2.7 GASMAS theory

2.7.1 Tunable Diode Laser Absorption Spectroscopy (TDLAS)

Tunable Diode Laser Absorption Spectroscopy (TDLAS) is a frequently used technique to detect the concentration of certain gas species, for example, oxygen (O_2), water vapour (H_2O), methane (CH_4) and so on. The principle is based on the Beer Lambert-Law where the laser frequency is tuned over a specific absorption line of a gas species, and the transmitted light is detected. The concentration of the gas is calculated through the following equation:

$$\begin{aligned} I(\upsilon) &= I_0(\upsilon)e^{-\alpha(\upsilon)\cdot L} \\ &= I_0(\upsilon)e^{-\sigma(\upsilon)N\cdot L} \ , \end{aligned} \tag{7}$$

where υ is the laser frequency, $I_0(\upsilon)$ is the irradiation intensity and $I(\upsilon)$ is the transmitted intensity; $\alpha(\upsilon)$ is called absorbance; $\sigma(\upsilon)$ [cm^2] is the absorption cross section of the species, N is the number density; and L is the optical path length that light propagates through the gas. However, due to the optical noise (mainly the shot noise which is the square root of incident photon number), or the noise from the detector (mainly the dark noise caused by the dark current), or due to optical interference from the optical set up (like back reflection into laser source), such a measurement is only limited to high absorption of gas, in which case the detected signal is not overwhelmed by the noise. In order to decrease the various sources of noise, some modulation techniques can be applied. In this thesis, wavelength modulation spectroscopy (WMS) is employed where the laser wavelength is fast modulated at a high frequency (kHz range), and when scanned over the absorption line, interaction between the absorption profile and the modulation will generate signal at higher harmonics of the modulation frequency.

2.7.2 Wavelength modulation spectroscopy

Wavelength modulation spectroscopy (WMS) is a common modulation technique where the laser frequency is modulated at a frequency typically in the range of $10 \sim 100$ kHz by fast tuning the inject-current of the diode laser. If the modulated laser is scanned around the species absorption profile, such an interaction becomes non-linear. This would generate a periodic signal at the laser modulation frequency and its harmonic frequencies.

If a higher harmonic signal is used to calculate the absorption, the so called $1/f$ noise can be dramatically decreased, and thus a higher SNR value is achieved. Wavelength modulation is characterised by a modulation frequency f_m which is much smaller than the width of the absorption peak (Γ_{HWHM}) of detected species, i.e. $f_m \ll \Gamma_{HWHM}$. Note that to achieve a stronger signal, the modulation amplitude should be set slightly larger than Γ_{HWHM} [26]. The difference between frequency modulation and wavelength modulation lies in the actual modulation frequency, where a much higher modulation frequency is applied for frequency modulation and the mathematical analysis of which is built on the phase modulation and the amplitude presented in the electrical field [27].

The general expression of the detected signal (under the condition that the absorption is very small) is described as:

$$\begin{aligned} S(\upsilon) &= \eta T(\upsilon) I_L(\upsilon) e^{-\alpha_0 \overline{\chi}(\upsilon)} \\ &\approx \eta T(\upsilon) I_L(\upsilon)(1 - \alpha_0 \overline{\chi}(\upsilon)) \ , \end{aligned} \tag{8}$$

where υ is the laser frequency, $S(\upsilon)$ is the detected signal and $I_L(\upsilon)$ is the output from diode laser; $T(\upsilon)$ is the system related transmission function, and normally it is wavelength dependent because of the equipment, like the tuning wavelength crystal or the APD amplifier; η is the sensitivity of detector; α_0 is the peak absorbance of detected species and $\overline{\chi}(\upsilon)$ is the peak-normalised line-shape.

The expression of the laser source modulation is described as:

$$\upsilon(t) = \upsilon_c + \upsilon_a \cdot cos(2\pi f_m t) \ , \tag{9}$$

where υ_c is the central frequency, υ_a is the modulation amplitude and f_m is the modulation frequency. Then the output intensity from diode laser can be expressed as:

$$I_L(t) = I_{L,0}(\upsilon_c) + \kappa_1 \cdot \upsilon_a cos(2\pi f_m t + \phi_1) \ , \tag{10}$$

where $I_{L,0}$ is the average intensity at the central frequency υ_c; κ_1 is the intensity-modulation coefficient which is characterised by the specific laser unit. What should be noticed is that the subscript 1 indicates the linear term of intensity modulation. In fact, the output intensity is not a perfect sinusoidal function, but with more terms which are nonlinear [27], t.ex, the second nonlinear term $\kappa_2 \cdot \upsilon_a^2 cos(2\pi 2 f_m t + \phi_2)$. However, these nonlinear terms of intensity modulation is not considered in our case because the modulation amplitude is small.

As we have mentioned before, a signal generated at higher harmonic of modulation frequency, the nf signal where $n = 1, 2, 3...$, is used to extract the gas absorption strength. One way to mathematically analyse the generation of nf signal is to decompose $T(\upsilon)$, $I_L(\upsilon)$ and $\overline{\chi}(\upsilon)$ in equation (8) into Fourier components, combined with the frequency modulation in equation (9). Detailed expression of $S_{nf}(\upsilon_c)$ can be seen in references

[26][27]. Figure 7 shows how the nf harmonic signal appears and we notice that the peak amplitude of the nf signal decreases as the harmonic frequency increases. So the $2f$ signal is most commonly used because it still maintain a relatively high amplitude compared to the other higher harmonic signal, while the $1/f$ noise has decreased a lot, compared to $1f$ harmonic signal.

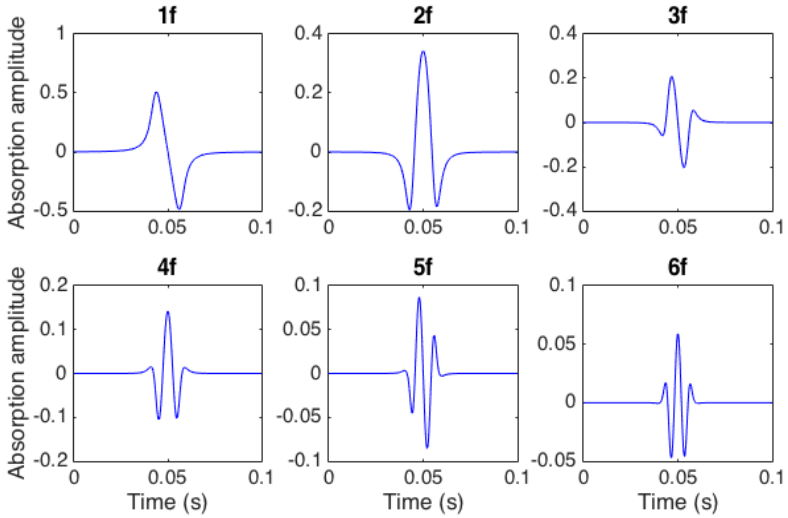

Figure 7: Figure shows the first six harmonic signal from a simulation result in [26].

2.7.3 GAs in Scattering Media Absorption Spectroscopy (GASMAS)

Gas concentration measurement that refers to TDLAS is a direct measurement technique where the optical path length is well known. So that the absorbance can then be directly calculated from equation (7). However, when light is propagating in a scattering medium, like tissue, the optical path length can no longer be treated simply as the distance between the laser source and the detector. Light is scattered, a process that can not be controlled and known, and thus the optical path length is unknown. So the GASMAS technique is introduced where an additional laser at wavelength λ_2 is used to probe the optical path length for the original laser at wavelength λ_1, and λ_2 is close to λ_1 in spectrum. In this thesis, the laser at $\lambda_2 = 935$ nm, to probe water vapour, is utilised. Given the relative humidity and the temperature, the concentration of water vapour can be determined, and the corresponding optical path length can be calculated from equation (7). It is assumed that oxygen and water vapour laser have a similar propagation behavior. In order to do measurements on both molecules at the same time, the 760 nm and 935 nm laser sources are modulated at different frequencies of 9015 Hz and 10295 Hz, respectively. Meanwhile they both have 5 Hz of ramp frequency to look for the their absorption lines. In that way, the absorption signal from oxygen and water vapour can be separated by applying a window in the Fourier spectrum of the detected signal.

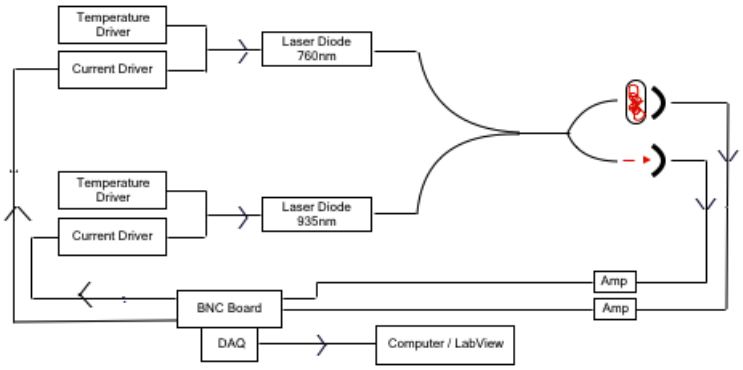

Figure 8: Both the oxygen detection diode laser at 760 nm and the water vapour detection diode laser at 935 nm are controlled by their own temperature and current drivers. The modulation of the injection current is connected to BNC board, from which we can manipulate the modulation on the computer. Two laser sources are merged into one fiber. Then one arm with most of the light goes to sample and the transmitted light is detected by a photon diode; while the other arm with less amount of light is the reference arm with known distance between the fiber tip and the detector. After amplification, signal is sent to BNC board and collected by DAQ card.

2.7.4 Signal processing

The basic concept of data processing [28] is to do the digital Fourier transform of the detected signal, select the signal generated at one or more of the harmonic of the modulation frequency and convert it back to time domain. Figure 9 shows the typical signal from GASMAS detection both in time domain and it Fourier spectrum.

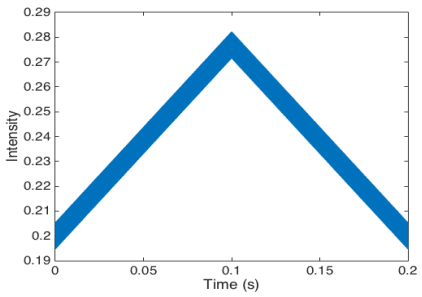

(a)

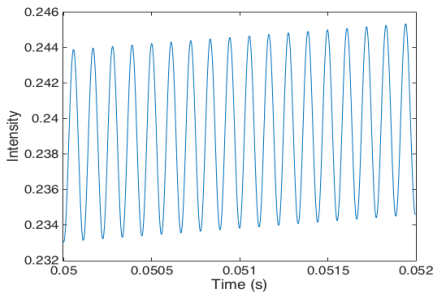

(b)

A super Gaussian window is utilised to filter out one of the harmonic signal, $S_{filt}(\upsilon)$, which can then can be expressed (in frequency domain) as:

$$S_{filt}(\upsilon) = F(S(\upsilon)) \cdot 2exp((-\frac{\upsilon - n_f \cdot \upsilon_{mod}}{df})^8) \ , \tag{11}$$

where the symbol F represents the Fourier transform, $n_f = (1, 2, 3...)$ is the number of harmonics that will be of interest and df is the width of the Gaussian window. The

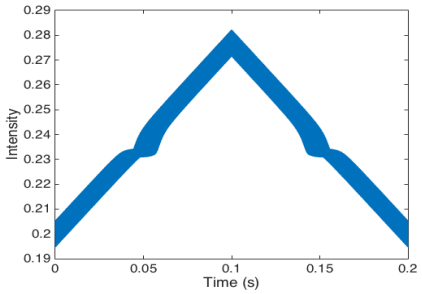

(c)

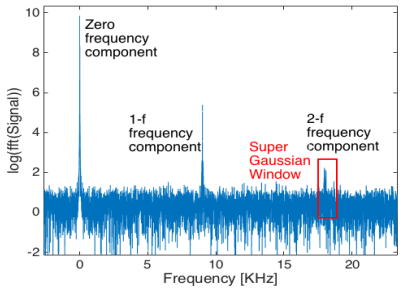

(d)

Figure 9: a)The typical incident light intensity in a period of scan. b) The zoom in of the modulation of light. c) The detected signal where the dip comes from the absorption of gas. d) The Fourier transform of the detected signal, where the peaks locate at the modulation frequency and its harmonic. The peak enclosed in the super Gaussian window, indicated by red rectangle, is the $2f$ signal.

selected harmonic signal is then down shifted tills it becomes the zero frequency. Because the amplitude of signal is represented at zero frequency, so that the strength of $2f$ signal can be extracted. Then we do the inverse Fourier transform:

$$S^*_{nf,filt}(t) = F^{-1}(S_{filt}(\upsilon + n_f \cdot \upsilon_{mod})) \ , \tag{12}$$

$S^*_{nf,filt}(t)$ is a complex signal (indicated by the star symbol) because the negative frequency is removed since the Gaussian filter window is only applied to the positive frequency. $S^*_{nf,filt}(t)$ is then phase adjusted and intensity normalised in order to get the signal amplitude that is directly proportional to the absorbance of the gas. Detailed calculation of these two steps can be seen in Appendix C.

2.7.5 Optical interference

One of the main interference is the etalon effect, originated from the accidentally-formed cavity because of the highly scatter medium where the light is back scattered into the laser through a fibre, or the coupling from diode laser to fibre. If the distance between the two surface of such a cavity is L, the free spectral range is $\upsilon_F = c/2nL$ where c/n is the speed of light. The light source intensity I that is incident on the scatter medium has now become [29]:

$$I = \frac{I_{max}}{1 + (2F/\pi)^2 \cdot sin^2(\pi\upsilon/\upsilon_F)}, I_{max} = \frac{I_0}{(1 - |r|^2)} \ , \tag{13}$$

where I_0 is the intensity of initial laser output; F is the so called finesse, defined as $F = \pi\sqrt{|r|}/(1 - |r|)$ and, $|r|$ is the magnitude of the round-trip attenuation factor, mainly determined by the reflection of the surface. For example, if the reflectivity of a surface is 0.04, the $|r|$ is calculated as $(0.04)^2 = 1.6 \times 10^{-3}$. Figure 10 shows how the

interference fringe, with different L and thus different υ_F, will affect the signal, given the finesse F equals to 0.04.

For a small distance of 10 mm, like the coupling distance between diode laser and fibre, the free spectral range is large according to equation (13). This will cause interference fringes at a low modulation, and it is the main reason for the offset to the signal baseline. However, for a much longer distance of 50 mm, like the distance from the sample surface through a fibre to the diode laser, the free spectral range is much smaller and thus has a much higher modulation. The caused interference is much easier to be averaged out.

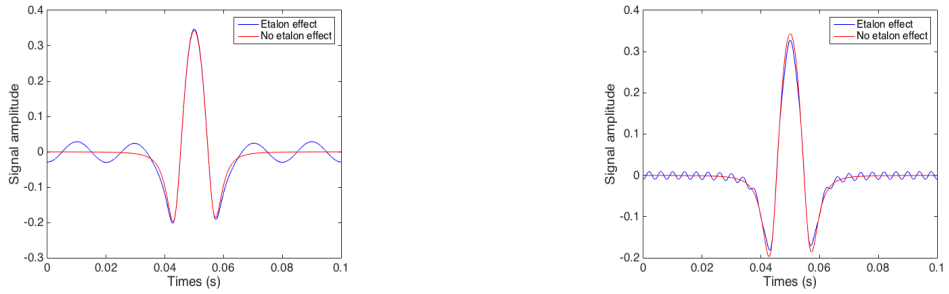

(a) (b)

Figure 10: a) The comparison of $2f$ signal between being affected by etalon effect or none when $L = 10$ mm with $\upsilon_F = 15$ Gz. b) The comparison when $L = 50$ mm with $\upsilon_F = 3$ Gz.

2.7.6 Signal calibration from reference arm

As has been mentioned before, the phase adjusted and intensity normalised $2f$ absorption signal is directly proportional to the gas absorbance $\sigma \sim C_{unknown}L_{unknown}$, t.ex. $S_a(t) = k \cdot \sigma \sim k \cdot (C_{unknown}L_{unknown})$, where k is a factor that is related to the laser output intensity, the wavelength-dependent system transmission and absorption line profile; $C_{unknown}$ and $L_{unknown}$ are the unknown oxygen concentration and optical path length in the lung, respectively. However, it is hard to calculate the k factor. Instead, a reference arm is used where the laser is incident on the detector through ambient air, meaning that the distance and the oxygen concentration are known. By this way, we can quantitatively obtain the amplitude of $C_{unknown}L_{unknown}$ from the sample signal by comparing the measured sample and reference signal, getting rid of the complex step of calculating the k factor.

$$\frac{\overline{S}_{ref}(t)}{\overline{S}_{sample}(t)} = \frac{k \cdot C_{ref}L_{ref}}{k \cdot C_{unknown}L_{unknown}} = \frac{C_{ref}L_{ref}}{C_{unknown}L_{unknown}} = G \ , \tag{14}$$

$\overline{S}_{sample}(t)$ and $\overline{S}_{ref}(t)$ are the detected signal that have been processed (see equations (11), (12), (19) and (20) in appendix C). G is a factor. In order to quantitatively

compare the signal from the sample and reference arms, the interference of etalon effect and the noise are taken into account. A second order Levenberg–Marquardt non-linear curve fitting algorithm is used:

$$\overline{S}_{sample}(t) = p_0 + p_1 \cdot t + p_2 \cdot t^2 + G \cdot \overline{S}_{ref}(t - t_0) \ , \tag{15}$$

t_0 is the shift parameter in case that there is drift in the temperature and current.

2.7.7 Equivalent path length from water vapour detection

Although we have calculated the amplitude of $C_{unknown}L_{unknown}$ from the reference signal, the value of $L_{unknown}$ still need to be calculated in order to determine oxygen concentration $C_{unknown}$. Given the assumption that the water vapour laser at 935 nm probes the same optical path length in the lung as the oxygen laser at 760 nm does, this path length, $L_{unknown}$, can then be obtained from the water vapour detection according to Beer-Lambert law. Because, unlike the oxygen concentration, the water vapour concentration can be analytically calculated if the relative humidity (RH) and temperature are known. RH is defined as the ratio of mole fraction of water vapour at moist atmosphere, X, to that at saturation condition, X_s, t.ex, $RH = 100 \cdot X/X_s$. Since the mole fraction is equal to the volume fraction, the water vapour concentration presented in ppmv can be expressed as:

$$\begin{aligned} H_2O(ppmv) &= 10^6 X = 10^4 RH \cdot X_s \\ H_2O(ppmv) &= 10^4 RH \cdot \frac{P_s(T)}{P_a} \ , \end{aligned} \tag{16}$$

The ideal gas law is applied to replace the X_s in terms of saturation water vapour pressure at temperature T, the $P_s(T)$, and the atmospheric pressure, P_a. According to [30], $P_s(T)$ can be expressed as:

$$P_s(T) = P_A \cdot e^{13.3185t - 1.9760t^2 - 0.6445^3 - 0.1299^4} \ , \tag{17}$$

where P_A is the standard atmospheric pressure of 1013.25 mb; t is a parameter defined as $t = 1 - T_s/T$, in which T_s is the steam temperature of 373.15°K at pressure P_a. By this way, the concentration of water vapour can be calculated if relative humidity can be known according to the current measurement environment. At room temperature T of 298.15°K, and atmospheric pressure P_a of 1000 mb, $P_s(T)$ is calculated as 31.38 mb. Typically the actual vapour pressure in air at room temperature is 10.2 mb, which in turns indicates a $RH = (10.2/31.38) \cdot 100\% = 32.5\%$. Therefore, the concentration of water vapour is calculated as 10197 ppmv, which is 1.02% in volume fraction (while oxygen in air is 21%). So combining the water vapour measurement on both sample arm and reference arm, the optical path length in lung can be achieved by using equation (14).

2.8 DICOM image

Digital Imaging and Communication in Medicine (DICOM) is an image format specific to medical digital images, like CT and MRI (Magnetic Resonant Imaging). Its standard was first established and specified by the American College of Radiology (ACR) and the National Electrical Manufacturers Association (NEMA), with the aim to build a platform for communication where information of image can be transferred. The scope and the field of application of this standard are mainly to do operation on network (on-line communication), and medium communication (off-line communication) supplied by devices that allow people to facilitate access to the stored medical images and related information.

In the thesis work, the most interest field is the data of images. DICOM consists a list of data attributes. Expect for the digital images themselves (resolution, physical dimension, scalar size), DICOM data structure also contains different fields, such as patient information like sex, age, weight, home address or identification number; or information about the modality, exposure time; or the image collection procedure such as acquisition time, direction cosine, implementation doctor etc.

2.9 Modeling Near-Infrared light transport in tissue

A software tool called Nirfast [31][32] is used in our study to model the light propagation in tissue, based on a numerical simulation through the Finite Element Method (FEM) [33]. Nirfast is a free open source and has a cross platform with Matlab, under which the simulation is performed. The input of Nirfast allows diverse formats of images, including DICOM images, which can be directly imported and the relative digital image information and medical information are also shown on the interface.

The application of Nirfast is mostly for segmenting medical digital images where different modular plugs can be used to classify different tissues. For example the plug of K-Means + Markov Random Field to Paintbrush (ITK), it is a modular tool that uses K-Means algorithms [34] to cluster gray scale values of a digital image. The Nirfast application also includes 3D mesh creation in which the mesh quality can be specified according to customer needs and the complexity of the segmentation. The light propagation simulation is based on the diffusion equation (see equation (3)), with available solutions of standard single wavelength absorption and scatter, fluorescence and multi-wavelength spectrally constrained solution. The standard single wavelength solution is used in this thesis.

During the Nirfast simulation work in the project, two main tasks are performed, namely CT image segmentation with Nirfast and detection geometry evaluation.

3 Methodology

3.1 Simulation Work

3.1.1 CT image segmentation with Nirfast

Two CT image series in format of DICOM are provided by the Lund University Hospital. First is for a 3.8 kg full term infant and the images were taken three days after birth. Secondly the images of a 1.7 kg preterm infant, born at week 33, were taken at thirteen days after birth. During the following description, only the procedure on the 3.8 kg is presented. Firstly, segmentation of these CT images is performed, which is the preparation before running a simulation of light propagation in this segmented model. Table 7 shows the necessary image information that is used as reference during segmentation, where image series is the total amount of image slices; voxel dimensions is the pixel numbers in an image slice; distance unit tells the real pixel scale, which is in millimeter; physical dimensions is the real size of an image slice; voxel spacing is the distance between two voxels, so the physical dimension is the product of voxel dimensions and voxel spacing.

Table 7: The information for CT images.

Image series	255
Voxel dimensions	$512 \times 512 \times 255$ voxels
Distance unit	mm
Physical Dimensions	$156 \times 156 \times 178.5$ mm
Voxel spacing	$0.304688 \times 0.304688 \times 0.7$ mm

In Nirfast, the display of images consists of four different views, the 3D full view, the sagittal view, the coronal view and the transverse view. When doing the segmentation, all of the latter three views can be used, depending on what one would like to do. The first step in the segmentation is to crop the CT images. As we are only interesting in the upper body, the parts below the diaphragm, where the liver and the intestine are situated, are discarded. The useless part around the body is also cropped away, by looking in the coronal plan. Image related information have then been altered to the values shown in table 8.

Table 8: The new information of DICOM image

Image series	146
Voxel dimensions	$512 \times 297 \times 146$ voxels
Physical Dimensions	$156 \times 156 \times 178.5$ mm

Step two is to interpret the CT images and clinical assistance is needed to distinguish

tissues, like skin, subcutaneous layer, ribs, muscle, bronchi, cavity, and alveoli. For simplification, we segment the alveoli, blood vessel and bronchioles as the same region, which gives the lung a complete homogeneity. And it is also out of the consideration of constructing a doable physical phantom. As a result, six regions are suggested, which are skin, fat, muscle, lung, heart and bone.

Step three is to the label these regions. The quickest way to do a rough segmentation is to use a plug of Threshold To Paintbrush. By doing it this way, we need to know the image intensity range (unit [HU]), which is the meaning of threshold in the plug. The intensity range for air and mattress is from -1024 (minimum) ~ -750. And for the six regions, the lung is from $-750 \sim -175$, fat from $-175 \sim -20$, skin from $-50 \sim 50$, muscle from $50 \sim 200$, heart from $200 \sim 575$ and bone from $575 \sim 3071$ (maximum).

Step four is to manually refine the rough segmentation, based on the rules that, firstly the segmentation should have the physical geometry, or shape, as close as possible to that of the raw images; secondly, there should be no un-segmented voxels within each region. An ideal segmentation is represented in figure 11:

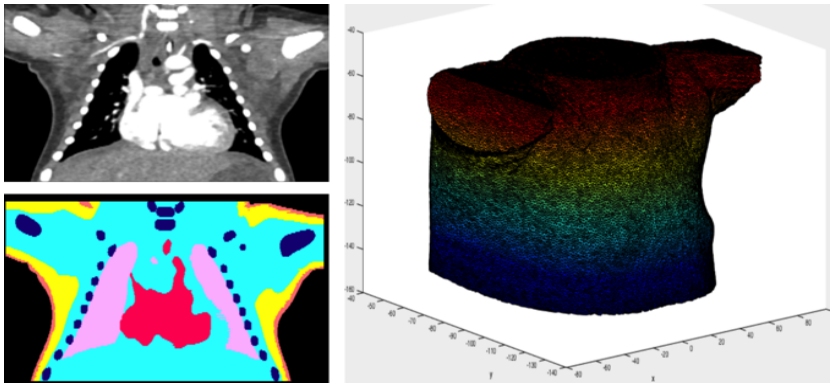

Figure 11: Figures on the left show the comparison between the raw CT image and the finished segmentation of different tissues labeled by different colors. The pink color indicates the lung, the red for the heart, the yellow for the fat, the orange for the skin, the light blue for the muscle and the deep blue for the bone. Figure on the right shows the created mesh.

Step five is to create a mesh according to the segmentation. The mesh is created with Matlab with the mesh setting shown in table 9. Tetrahedron size in unit of millimeter is the upper bound for the circumradius of a tetrahedron, and a better tetrahedron quality will give a better simulation of light propagation. The size of a surface facet of a tetrahedron should be the same as the tetrahedron size. The angle determines the angle between two facets (a tetrahedron has four facets in total). And the distance controls the approximation error of the boundary. The created mesh can be seen in figure 11.

Table 9: The parameter setting during mesh creating.

Mesh type	Standard	
Tetrahedron setting	Tetrahedron size (mm)	1.0
	Tetrahedron quality	3.0
Surface facet setting	Size(mm)	1.0
	Angle(deg.)	25
	Distance (mm)	3.0

Step six is to place the source and detector points. From previous clinical trial experience (at least for big infants) [1], the source and the detector are put in front of the chest or by the side, and they can not be separated too far away. Because the detected signal is very week. So 27 points have been placed only around the left lung on 6 different slices of identity 30, 40, 50, 60, 70 and 80, with 7 mm in separation in the z-axis. On average there are 5 points sitting at each of these slices. See figure 12 where we can see the points are fully detecting the left lung. These points play the role of source, and meanwhile the detector. For example, when the point 1 (which sits at the bottom right corner at slice 30) is the source, including itself and the rest 26 points are the detectors. When the source changes to point 2, the rest 26 points and itself would be the detector, and so on. Therefore, in total there are $27 \times 27 = 729$ measurement geometries, and thus 729 solutions. It should be noticed that no matter which point is the source, the detection sequence would always start from point 1 to point 27, according to the sequence how the points are placed.

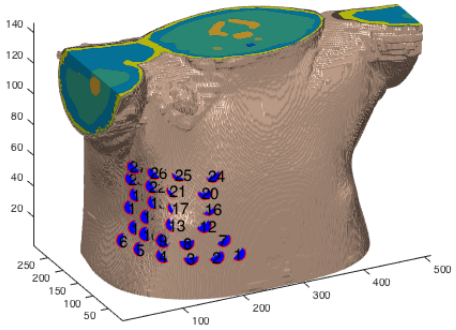

Figure 12: The blue points in the figure are the source points as well as the detector points. The number beside each point indicates the identity.

Step seven is to assign optical properties which has been determined and shown in table 6, The last step eight is to run a standard solution.

For the segmentation of the 1.7 kg infant, the process is almost the same as the 3.7 kg infant. The only difference occurs in step three where different tissue types are identified. The intensity range is distributed differently where the skin and lung have the intensity range of $-650 \sim -150$, fat of $-150 \sim 0$, muscle of $0 \sim 400$, heart of $400 \sim 600$ and bone of $600 \sim 3031$. The mesh creating has the same parameter setting.

As to the placement of the source and detector, the strategy is also to put them around the left lung. 16 measurement points are placed, with an approximate separation of 15 mm between two adjacent points. This gives $16 \times 16 = 256$ solutions in total. See figure 13 about the segmentation and position of these measurement points:

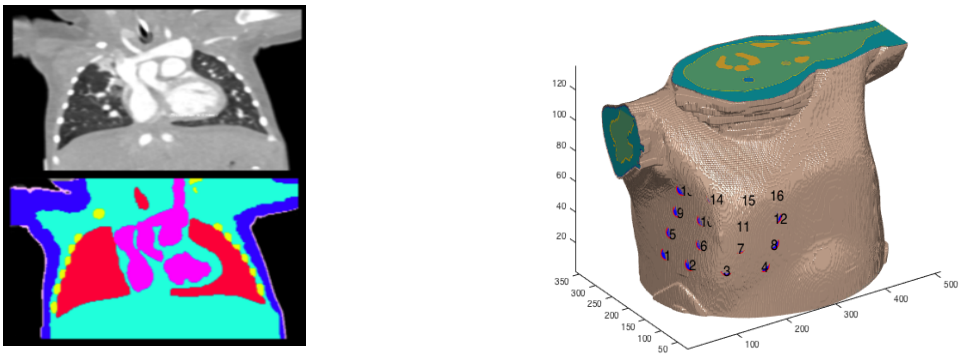

(a) (b)

Figure 13: a) A slice of the raw CT image of the 1.7kg infant and below that is the segmentation of different tissue. The red color indicates the lung, purple for the heart, yellow for the bone, pink for the skin, light blue for the muscle and deep blue for the fat. b) The blue points are the source points as well as the detector points. The number beside the points indicates the identity.

3.1.2 Detection geometry evaluation

One of the main purposes of the simulation is to find the best probe-detection geometry that can let the light propagate as much as possible in the lung while maintaining a detectable transmitted intensity. In that way a relatively large amount of gas can be probed, giving a stronger absorption signal. So taking the advantage of automatic simulation done by a computer, we put 27 measurement points as the laser sources and detectors all around the left lung (figure 12). We can statistically compare the 729 solutions and decide which solutions are the preferable for practical measurement geometries. By doing so, when it comes to practical measurement, we can save dramatic effort.

However, in Nirfast, it is hard to know how long distance that light has propagated in the lung. Instead, we measure the response of the transmitted light due to the change of optical properties of the lung, which is defined as the sensitivity δ. Only the absorption coefficient is changed because then it can be assumed that the light propagation trajectory in two independent simulations are the same if the scatter events stay unchanged, which is determined by the reduced scattering coefficient. The sensitivity is defined as:

$$\delta = \frac{I_{\mu'_{a,lung}} - I_{\mu_{a,lung}}}{I_{\mu_{a,lung}}} \ , \tag{18}$$

where $I_{\mu_{a,lung}}$ is the detected transmitted light before μ_a is changed and $I_{\mu'_{a,lung}}$ is after μ_a is changed. Two group of simulations are done, one of which, group 1, with $\mu_{a,lung} = 0$ cm^{-1} and $\mu'_{s,lung} = 0.1$ cm^{-1}, and the rest of the optical properties for the other tissues are taken from table 6; while for group 2, it has $\mu_{a,lung} = 0.6$ cm^{-1} and $\mu'_{s,lung} = 0.1$ cm^{-1}, the rest of the optical properties remain the same. The reason why to use different lung optical properties from the table 6 is that in lab measurements, the lung is filled with ambient air which does not have scattering and absorption properties (except for the gas absorption which is small compared to tissue absorption). When running the simulation, the scattering properties can not be set to zero according to the definition of the diffusion equation. So the scattering coefficient is set to a small value.

A high value of δ may indicate that the light under that measurement geometry is probing more of the oxygen in the lung. But we still need another criteria that the transmitted light should not the too low to be detected, or the SNR should be typically larger than 3 [1]. In Nirfast, the default laser power is 1 W. Assuming a detection limit of one photon in ten thousands, we should select those measurement geometries who have the amplitude of $I_{\mu_{a,lung}}$ ($\mu_{a,lung} = 0$ cm^{-1}, $\mu'_{s,lung} = 0.1$ cm^{-1}) larger than 1/10000.

3.2 Computer file for 3D phantom printing

To make a robust and physical phantom, it should have similar structures to an infant. Based on the segmented images, only the boundary of the organs of interest (the skin, fat, muscle, heart and bone) is 3D printed as the shield, where liquid phantom with desired optical properties is filled in. We should notice that these six regions have their own constant intensity displayed on these segmented image. These segmentation images can be directly exported as a series of images of different format such as .JPG or .PNG. Taking the case of 3.8 kg infant for instance, these exported images are combined as multi frames to become a three dimensional array of size $297 \times 512 \times 146$, where 146 is the total number of the CT series. One important step is to assign the voxel spacing parameters (shown in table 7) to the array in order to have the same true physical size as the infant. The boundaries of these regions, or the surface in generally, can be simply extracted with the Matlab function [vertice,facet] = isosurface (3D array,isovalue) where the isovalue represents the intensity of the different regions. The surface-extracted array is then input to a code program that converts a 3D logical array to .Stl file, which is a common used format for a 3D printer. The program is written by Sven Holcombe [35].

The 3D printer available, EOS Formiga P110 selective Laser sintering system, located at Ingvar Kamprad Design Center (IKDC), prints using nylon. The printing procedure is done with the help of Jonny Nyman[5] from IKDC. The working principle is that by spreading a layer of nylon powder onto the platform, a laser is used to melt the powder according to the shape of the slice of customers' model. Then the platform drops down

by 0.1 mm, and another layer of powder is spread on top of the first one. The process repeats until the model is finished. In our case, the bone is printed as solid because of its complex structure and small size. The remaining issue to considered is the wall thickness of the lung, heart and fat layer. Ideally, the thinner the wall thickness, the better it gets close to the segmentation of image. However, as we have mentioned that the CT images are taken every 0.7 mm of the body, the modeling of the surface of these organs would therefore not be continuously smooth. A certain wall thickness is needed to support the connection between two consecutive layers (images). On the other hand, considering the optical properties that the absorption coefficient for nylon is 0.02 cm^{-1} and the reduced scattering coefficient is 46.5 cm^{-1} (see table 6 in section 2.6), a thin wall with a thickness below, for example 1 mm, may not affect the light absorption. However the introduced light scattering and reflection by nylon needs to be determined. So for the first stage of the project, at least we should make sure there is no leakage when we fill these models with liquid. We decide to make the thickness of 0.5 mm for the lung and heart; and 0.7 mm for the fat layer in order to hold the amount of liquid phantoms of fat and muscle. Meanwhile it can prevent presence of tiny holes on the surface which may lead to leakage. The same thickness decision has also been applied for the 1.7 kg infant.

3.3 Preparation of liquid phantom

At first, we have to determine the optical properties of the Indian ink (brand: Pelikan, made in Germany) and the intralipid of 20% suspension (brand: Sigma, phospholipid stabilized soybean oil) used during the laboratory work. Measurement on the ink absorption coefficient is implemented by the collimated transmittance system (see figure 14) where collimated white light passes through a cuvette (size of 1 cm width) of water and ink solution, and the focused transmitted light is sent to a spectrometer. A proper exposure time should be used and changed according to different ink concentrations, in order not to let the transmission light saturate the spectrometer. The sample measurement is calibrated by a measurement on a cuvette of water only. In order to obtain a reliable value, the transmission should not be too low to be overwhelmed by background noise; and should not be too high which can reduce the spectrum resolution, covering the detailed information at some specify wavelength; the transmission should be in the range of $1\% \sim 20\%$. Two cuvettes with concentration of 2.5% (transmission of 16.21%) and 4.8% (transmission of 2.83%) are used and the measured μ_a at 760 nm are 1.619 cm^{-1} and 3.163 cm^{-1}, respectively, which leads to real absorption coefficient of ink of 64.76 cm^{-1} and 66.04 cm^{-1}. For the ink that is used during the measurement, it is already diluted into a suspension of 1%, which means that the measured μ_a for 100% ink is approximately equal to 6540 ± 64 cm^{-1}, close to the literature value [23] of $\mu_{a,ink} = 6490 \pm 30$ cm^{-1}.

[5]Home page: http://www.design.lth.se/om-institutionen/verkstaden/vem-goer-vad/?L=2

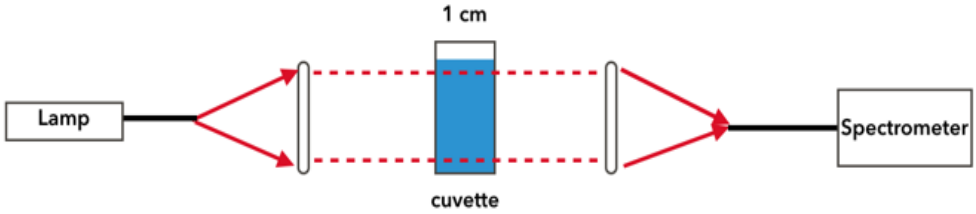

Figure 14: The white light source from a lamp is collimated by a lens, and it passes through a cuvette of width 1 cm, where the sample is. The transmitted light is focused and sent to a spectrometer.

Concerning the measurement on the intralipid of 20% suspension, we diluted 40 ml of the intralipid into 360 ml water and stir it for 30 minutes and measured the optical properties in an infinite geometry where fibers are deep into the solution, with the PTOF system. The result shows $\mu_s' = 20.0001$ cm^{-1} of this 10% solution, which is the same as the literature value [25] of $\mu_s' = 200$ cm^{-1} for 100%. The corresponding μ_a is equal to 0.038 cm^{-1}, which means that the lipid also absorb a certain amount of light due to the oil component. Comparing to the absorption of the ink, this is negligible.

Now the optical properties of intralipid of 20% suspension ($\mu_s' = 200$ cm^{-1}) and Indian ink ($\mu_a = 65$ cm^{-1}) have been determined. For simplification, the absorption of the liquid phantom is only considered from ink and the scattering is only from intralipid, and the optical properties of water in not considered. Table 10 shows the ratio of mixing these three materials in order to achieve the optical properties shown in the table 6.

Table 10: The recipe of mixing liquid phantoms

Organ	Total volume (ml)	Water (ml)	Intralipid (ml)	Ink (ml)
Fat	300	284	15	0.46
muscle	500	279	18.8	2.18
heart	300	292	7.33	1.33

Once we have acquired the correct amount of material, the most important step is to apply the ultrasound application to the ink. Because the absorption properties can be significantly changed if the large carbon chains of pure ink are not decomposed sufficiently [24]. The intralipid should also be stirred homogeneously. These two things should be done separately, both for approximate 30 minutes. Note that no liquid phantom is made for the lung, because at the first stage measurement, the lung is empty with only air at atmospheric pressure (21% of oxygen).

3.4 Experiment with GASMAS system

The ramp frequency for both laser sources are 5 Hz, while the 760 nm oxygen laser has a modulation frequency of 9015 Hz, and 10295 Hz for the 935 nm water vapour laser.

The data is collected at a sampling frequency of $4,000,000$ Hz, meaning that 80000 data points in one ramp scan period are recorded. Before implementing measurements, some parameter of the laser modulation, like the ramp amplitude and the wavelength modulation amplitude, should be modified in order to detect as high signal as possible. This is done by doing a measurement on a polystyrene foam with a thickness of 5 cm. See figure 15. The water vapour and oxygen signal come from the gas inside the porous structure of the foam. First, an absorption line with highest peak should be used and this is found by fine-tuning the temperature controller, which would cause the laser central frequency to shift because the temperature determines the band gap of a semiconductor. After locating the strongest absorption line, the ramp amplitude should be set to a large enough value to scan over the whole absorption line. According to the description of Wavelength Modulation Spectroscopy (WMS) [26], the highest $2f$ absorption signal can be achieved when the modulation amplitude is 2.2 times larger than the Γ_{FWHM} of the absorption line. Since we do not know the line width of the absorption line, the modulation amplitude is approximately optimised by observing the peak of the detected $2f$ signal when changing the modulation amplitude step by step. To suppress interference fringes caused by the etalon effect, mechanical vibrators are employed. Under the vibration, the two surfaces of the accidental formed 'resonator', which are the sample surface and the diode laser exit, can be misaligned and so that the fringes get averaged out.

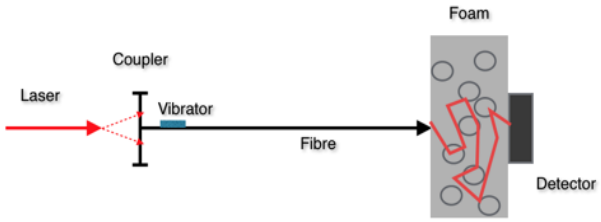

Figure 15: The laser output from the diode laser exit is coupled into a fibre through the coupler (a focus lens); a vibrator is tighten on the fibre near the coupler;

3.4.1 Sample arm measurement

To make sure the lung is filled with air, or to control the oxygen concentration, a hole is drilled on the bottom of each side of the phantom lungs. Then a transparent pipe is connected and at the same time, it seals the hole in order not to let the liquid leak into the lung. About the measurement itself, the measurement geometry follows the simulation result about how to place the laser source and the detector (see figure 24). Both the placement of the source and the detector should be close to position of the points that are marked on the skin surface (see figure 12 and 13). During the measurement, the interference fringes can be maximally suppressed by averaging signal for hundreds of time. Measurements are done on both the 3.8 kg and 1.7 kg infant models.

Normally, the detected absorption signal of oxygen is much weaker than that of water vapour, because the absorption imprint from oxygen is much weaker. A higher detection gain should be used in order to get a high SNR for oxygen signal. However, on the contrary, this would cause water vapour signal to saturate at such a high gain, if both laser are switched on at the same time. So when doing the measurement, either to choose a lower gain in order not to saturate both the signal, or to do the measurements on these two gases separately.

3.4.2 Nitrogen flushing measurements

In order to make sure the oxygen and water vapour absorption signal come from the lung, pure (100%) dry nitrogen is used to flush the lung of the 1.7 kg infant because it is easier to observe the change of signal due to the smaller size of model. 5 measurement geometries (source,detector) of $(5, 3)$, $(10, 3)$, $(12, 3)$, $(8, 6)$ and $(15, 6)$ are selected according to the sensitivity, from high to low values. Since it is difficulty to place the source or detector to its previous position after removing it, so the nitrogen is flushed right after the measurement is done in atmosphere condition for one measurement geometry so that the source and detector are still at their original position. Then the source or detector are moved to the next measurement geometry and air and nitrogen are flushed successively and the procedure is repeated. Two groups of the same measurement, group 1 on 06-Apr-2016 and group 2 on 09-Apr-2016 are done to do comparison.

In case there is oxygen and water vapour absorption coming from the bubble in these liquid phantoms of the fat and muscle, GASMAS measurements are also done on them. See figure 16. The heart liquid phantom is not considered since the amount is relatively very small and the heart model is located in the middle of the body, behind the lung, so the bubble effect from the heart could be neglected.

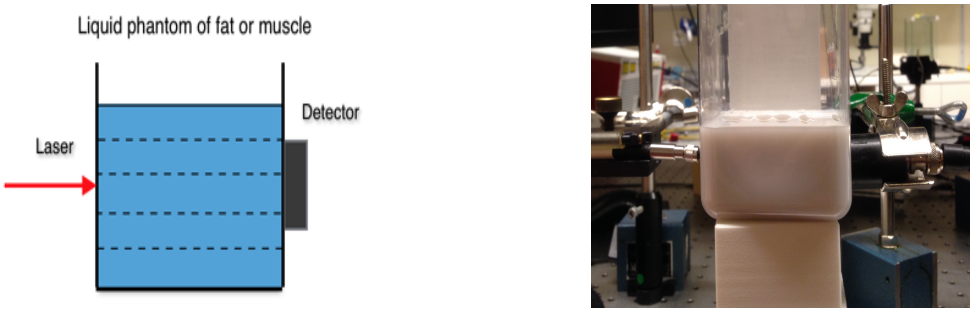

(a) (b)

Figure 16: a) A drawn set-up on how to do the GASMAS measurement on the liquid phantom of fat and muscle: the liquid is in a transparent plastic bottle where the fibre and the detector are attaching the surface of the bottle.b) The set-up in the lab that is identical to the drawn set-up.

3.4.3 Reference measurement

Measurement on the reference arm is implemented in order to calibrate the true optical path length that light has traveled in the lung. The laser source from a fibre tip is first collimated with a lens and then directly incident on the detector after passing through ambient air. It is difficult to collimate both laser beams at the same time because the water vapour laser beam is exiting from the center of the fibre core while the oxygen laser beam is exiting slightly away from the core center. So the reference arm measurement on water vapour and oxygen absorption are implemented separately. For the water vapour laser beam, it is not well collimated and when it arrives at the detector, the beam spot is larger than the 10×10 mm^2 size of detector. This is not a problem because the laser power is not high and the detector only sees the light going straight. The separation between the source and detector is 1201 mm. The thickness of the collimated lens is 5 mm and it is called the offset path length. So the true L_{ref} for the water vapour reference measurement is 1196 mm (figure 17a). For the oxygen laser beam, since the fibre can be taken away, so the light directly from the diode laser is collimated by another lens with a thickness of 2 mm to a spot smaller than the size of detector. The true L_{ref} for the oxygen reference measurement is 983 mm (figure 17b). When doing the reference measurements, the laser wavelength modulation parameters setting should be the same as that of the sample measurements. The signal is collected at an average of 200 times, and 5 groups of the averaged signal are recorded.

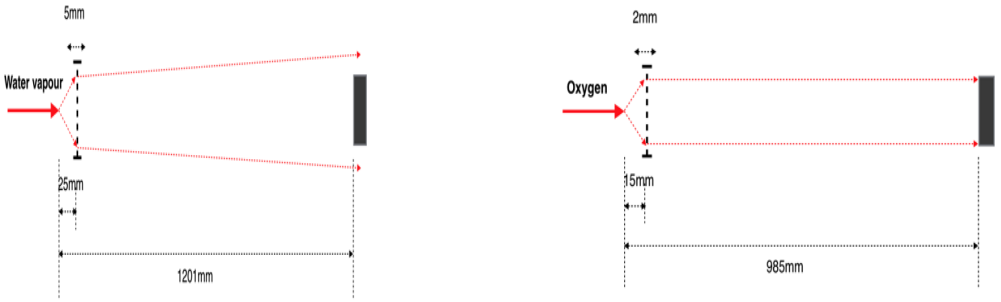

(a) (b)

Figure 17: In both figure the thick red arrows indicate the laser source; the black blocks indicate the detector and the vertical lines are the lens used to collimate the laser beams. a) and b) show the reference arm set-up for the water vapour and oxygen, respectively.

4 Result

4.1 3D printed model

Four tissues of lung, heart, bone and fat are printed individually. The fat tissue layer is enclosed by two surfaces, in between the liquid phantom of fat is filled. The bone is printed as solid while the lung and heart are hollow. No muscle model is needed to be printed because the muscle liquid phantom is embraced by the fat layer. Since the skin is so thin for a newly born infant, less than one millimeter, and even thinner for a preterm infant, it is difficult to print the skin layer. So the skin layer is temporarily not considered in this thesis. Figures of the digital models in the Matlab and pictures of the printed models from a 3D printer for the 3.8 kg infant can be seen in appendix A.

4.2 Liquid phantom optical properties

Table 11 shows the measured optical properties of the liquid phantoms according to table 10. However, it is difficult to mix the liquid phantoms to have the same optical properties each time. But a close value is guaranteed.

Table 11: Measured optical properties with PTOF system. The measurement geometry is infinite geometry where the fibers of sending and collecting light are deep into the liquid phantom. The separation of the fibers is 2 cm.

	Measured value		Ideal value	
	μ_a, cm^{-1}	μ_s', cm^{-1}	μ_a, cm^{-1}	μ_s', cm^{-1}
Fat	0.114	11.5	0.1	10
Muscle	0.276	8.5	0.287	7.49
Heart	0.276	5.05	0.284	4.89

4.3 Nirfast simulation

Simulation results from the 3.8 kg infant model (figure 18) are presented as intensity plot for source positions 1, 6 and 18 (figure 12) and the 27 detector positions. The spatial distance between each source and detector position is calculated based on the Cartesian coordinate system. The first point that indicates a minimum source-detector separation of 0 mm in the graphs of figure 18 is when the detector is overlapping with the source postion.

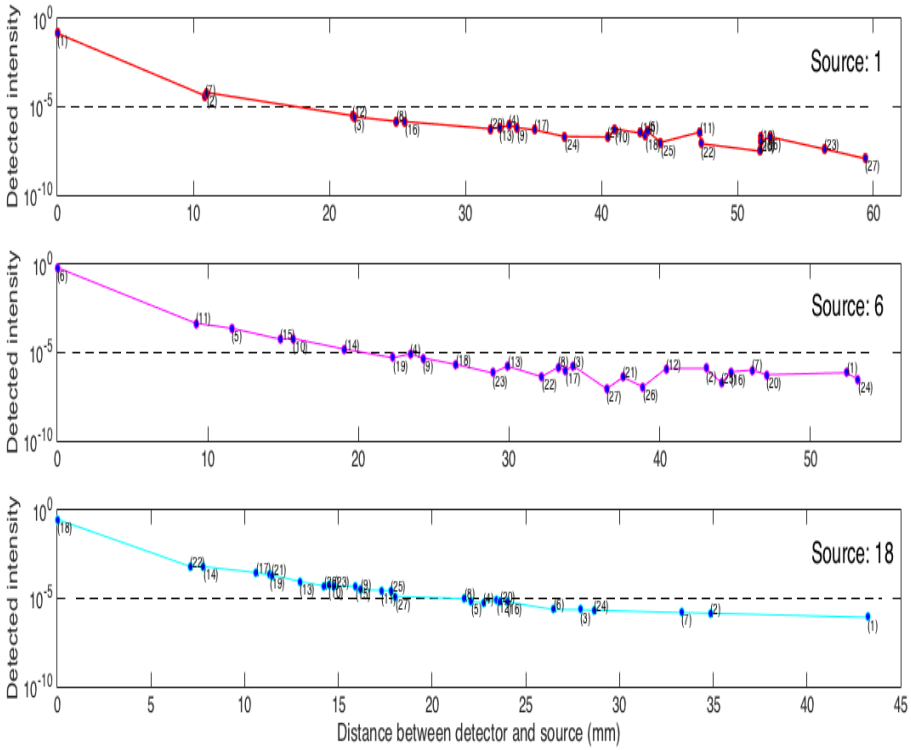

Figure 18: The graph on the top shows a plot (indicated by red solid line) of detected intensity versus source-detector separation, in which the source is placed at point 1. The number displayed in parenthesis is the identity number of each detector. The dash line is the threshold plot, which is a horizontal line at intensity value of 0.0001. The graphs in the middle and the bottom are for the cases when source is point 6 and 18, respectively.

From the simulations we observe that for further the separation, lower intensities are detected, which is to be expected. However, not all the combinations of source-detector pairs can be used. The detected amplitude should be larger than the detector limit (threshold), which is defined as 0.0001. From the three plots (figure 18), we notice that when the source-detector separation is approximately larger than 20 mm the detected intensity is below the detection threshold. From this result, it is suggested that when doing the GASMAS measurements, there is no need to have a source-detector separation larger than 20 mm. The threshold of 0.0001 is just an assumption and by using this value, 465 out of total 749 source-detector pairs are discarded. Considering that in the experiment the laser source and detector are separated, 27 source-detector pairs where the detector is overlapping with the source can also be discarded. So only the remaining 257 source-detector combinations are considered.

Recall that except for the criteria of the detective limit, another important consideration when choosing measurement geometry for the GASMAS measurements is that the detected light should have passed through the lung as much as possible. Figure 19 shows the sensitivity of the source-detector pairs versus the source-detector separation

for source position 18.

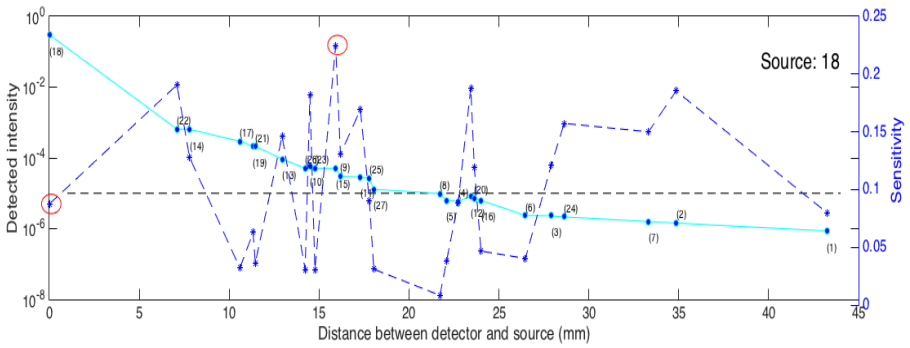

Figure 19: The left y axis is the detected intensity, the right y axis is the sensitivity value; the x axis is the source-detector distance; the blue dash line is the sensitivity plot.

It is clear that a high detected intensity does not correspond to a high sensitivity which means that the sensitivity value is not related to the intensity. Instead the sensitivity of light to the lung is dependent on the position of the source and the detector. For example, detector position 18 in the sensitivity plot (figure 19), its value is relatively low because the light detected does not propagate too much inside the lung. As a result, changing the optical properties from $\mu_{a,lung} = 0.00$ cm^{-1} to $\mu_{a,lung} = 0.06$ cm^{-1} does not affect the detected intensity too much. This could be that the source-detector separation is not far enough, or could be that the light coming from this source position is not even passing through the lung. However, for the detector point 9 (figure 19), the sensitivity value is high, but the intensity is weaker compared to detector point 18. This could be caused by a large source-detector separation. A graphical representation for light propagation inside and outside the lung is presented in figure 20.

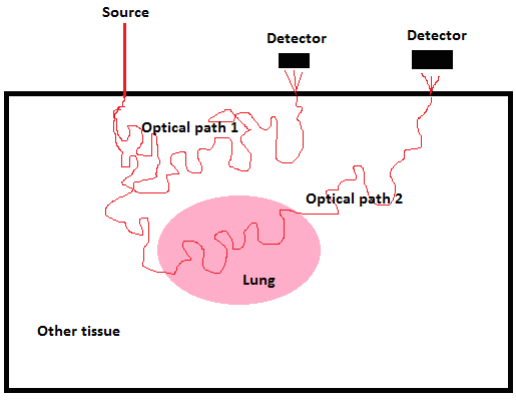

Figure 20: The pink circle represents the lung, and the rest white area is the surrounding tissues. The trajectory of optical path 1 does not pass through the lung, and the light is collected by the detector close to the source; the other trajectory of optical path 2 passes through the lung, and the light is collected by the detector far from the source.

Nevertheless, figure 20 does not indicate that a far source-detector separation would correspond to a high possibility for the light to pass through the lung, and thus a high sensitivity value. Figure 21 shows the distribution of sensitivity values along the source-detector separation. The sensitivity values from source points 10, 13, 17 and 22 (figure 21a) all have an evenly distributed sensitivity along the source-detector separation. It is clear that the sensitivity is independent from the source-detector separation when all the sensitivity values are plotted from the 27 source points (figure 21b).

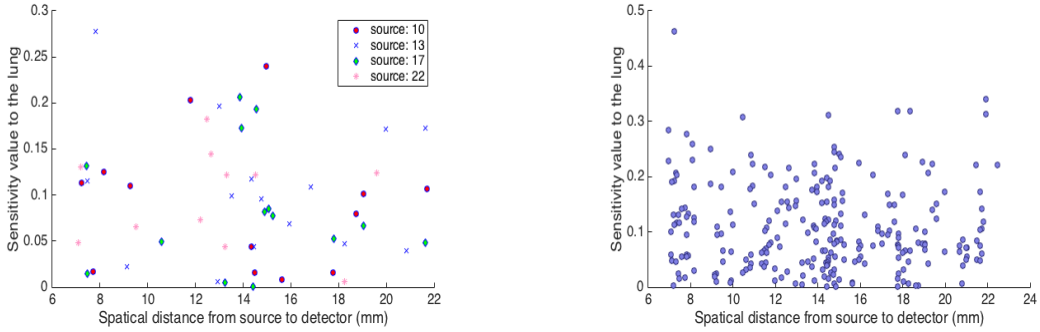

(a) (b)

Figure 21: The figures show how the distribution of sensitivity values to the lung is at different source-detector separations. a) The result from four source points. b) The result from all the source points.

The sensitivity is therefore not dependent on either the detected intensity amplitude or the source-detector separation, but is related to the position of the source and the detector. Then in the precondition of that the detected intensity is above the threshold, it is the amplitude of the sensitivity that decides the measurement geometries of interest. However, 257 measurement geometries would still be difficult to implement in a real measurement due to time constraints. Sensitivity values of the 257 source-detector pairs that are below a threshold, for example, $\delta_{min} = 0.05$, is discarded. This results in a remaining of 188 measurement geometries that should be tested first. Moreover, due to that the size of our detector (10×10 mm^2) in the experiment is different than the simulation where the detector is a point, the source and the detector can not be placed too close to each other. Therefore, it is decided to only select those source-detector pairs whose separation is larger than 15 mm. This leaves a remaining 72 measurement geometries. In fact the surface where we put the sources and detectors around the left lung is not flat, but it is curved, so 15 mm in the spatial separation between two points is equivalent to a larger separation along a curved surface. Figure 22a shows the best measurement geometry when the source is at point 4 and the detector is at point 12 for the 3.8 kg infant model.

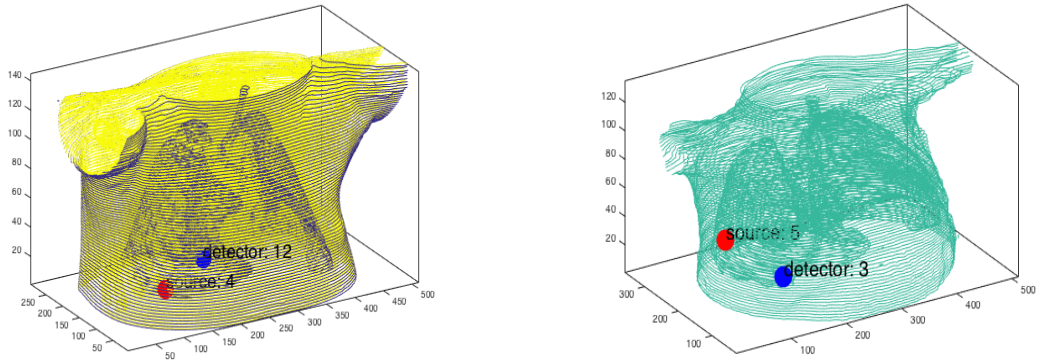

(a) (b)

Figure 22: The figures show how the best measurement geometry looks like. For the 3.8 kg infant (figure a), it uses point 4 as the source and point 12 as the detector, with the highest sensitivity of 0.3403; for the 1.7 kg infant (figure b), it uses point 5 as the source and point 3 as the detector, with the highest sensitivity of 0.3116.

As been mentioned before, the surface is curved while the detector surface is flat. So the detector can not be placed on a curved surface, ans this is illustrated in figure 23a. Only those positions where the detector is attached seamlessly (figure 23b) can be used in order to get rid of the oxygen and water vapour absorption that are not related to the lung. On the contrary, the laser source comes from a fibre tip, which is much easier to be placed on either curved or flat surface. So the choice of measurement geometry should be based on the convenience of attaching the detector.

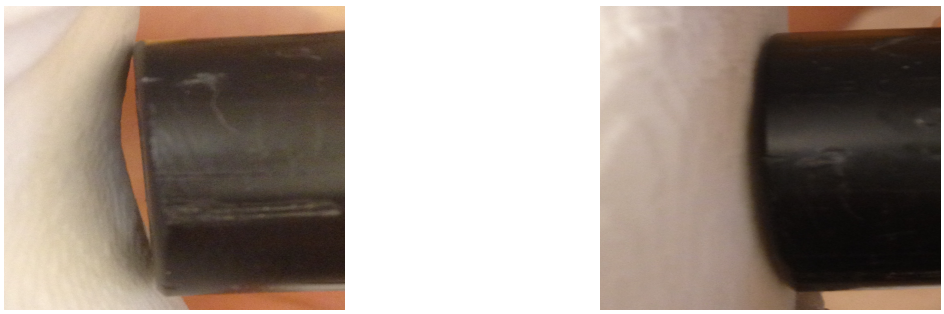

(a) (b)

Figure 23: a) The detector placed on a curved surface where in between filled with ambient air. b) The detector is firmly attached on the model surface.

This results in that the available detector positions are point 1, 2, 3, 7, 8, 12, 16 and 20 for the 3.8kg infant model. The finally decided measurement geometries for the 3.8 kg infant is shown in figure 24a, where the selected geometry is highlighted in red diamonds.

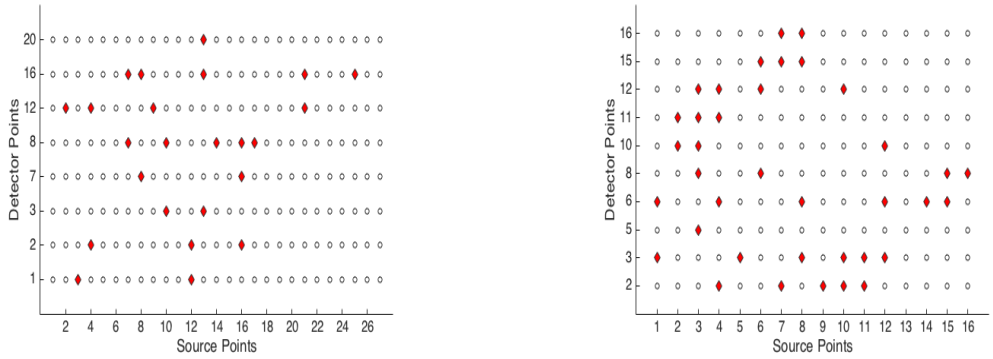

(a) (b)

Figure 24: The figures show which source-detector pairs, indicated by red diamonds, could be used in practical GASMAS measurement. The x and y axis represent the source and detector identity, respectively. a) The to-be-used measurement geometry list for the 3.8 kg infant. b) The case for 1.7 kg infant.

The simulation results for the 1.7 kg infant model is analysed in the same manner as the 3.8 kg model. But 51 geometries out of the total $16 \times 16 = 256$, are left after only considering the intensity threshold and a source-detector separation limit of 15 mm. Instead, all of the possible measurement geometries are implemented, which means that a sensitivity limit of $\delta = 0.05$ is not applied for this smaller infant model. 16 points are placed on the surface while points 1, 4, 7, 9, 13 and 14 are not used as detector points because of the curving surface problem. Consequently, the result of the to-be-used geometry list in GASMAS measurement can be seen in figure 24b.

4.4 GASMAS measurement

4.4.1 Reference measurements

Figure 25 shows the extracted $2f$ absorption signal of oxygen and water vapour, respectively, from the reference measurements. The super Gaussian window, used to extract the absorption signal at the second harmonic of modulation frequency, has a width of 600 Hz. The signal to noise ratio is good in both reference measurements. The baseline in the middle between the two peaks of the $2f$ oxygen signal is better than that of the water vapour which has a slightly larger offset from 0, caused by optical interference.

4.4.2 Sample measurements

For the measurements on the 3.8 kg infant model, the oxygen signal is too weak to be detected. Only water vapour is detected because of its much higher peak absorbance amplitude of the absorption profile, and a much higher laser power, compared to the oxygen molecule and the diode laser used for oxygen detection. Therefore, the GASMAS measurements results and discussions will only be presented for the 1.7 kg infant model,

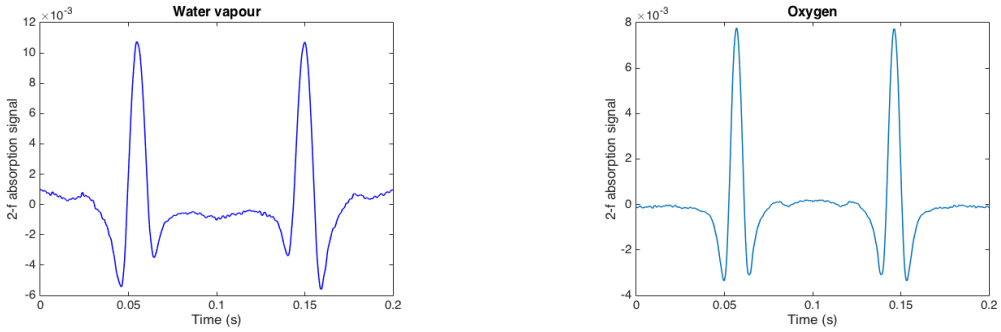

(a) (b)

Figure 25: Figures show the measured $2f$ absorption signal from the reference measurements. a) Water vapour. b) oxygen.

in which the detection of oxygen is possible. As a result, both the oxygen and the water vapour absorption signal can be detected on most of the measurement geometries (figure 24b), excluding (source,detector) pairs of $(3, 11)$, $(8, 16)$, $(8, 3)$, $(16, 8)$, $(7, 15)$, $(4, 12)$, $(3, 8)$, $(10, 2)$, $(8, 15)$, $(14, 6)$ and $(1, 6)$ that can not be measured due to the large dimensions of the detector and the fibre. Only data from 26 measurement geometries are available. The absorption path length in the lung is calculated from the fitting of the reference signal to the sample signal (equation (14)), by assuming that the oxygen concentration in the lung is the same as that in the air ($C_{unknown} = C_{ref}$). Figure 26 shows the oxygen absorption path length for each measurement geometry. They are sorted and plotted according to the sensitivity, from largest to smallest (figure 26a), or according to the source-detector separation, from shortest to longest (figure 26b), respectively.

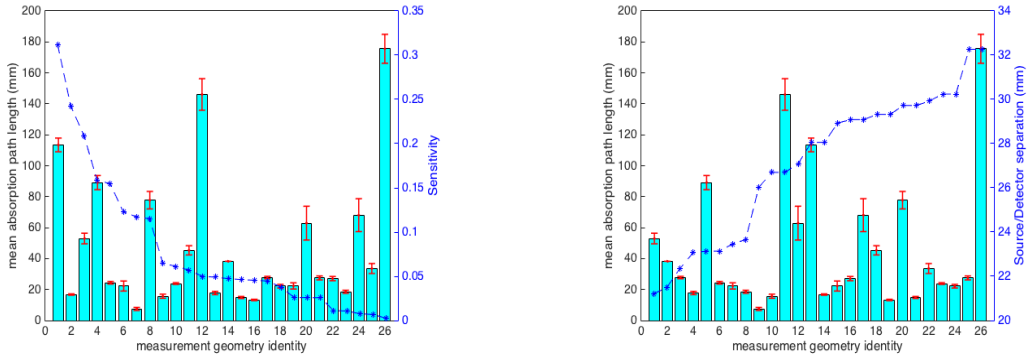

(a) (b)

Figure 26: a) The oxygen absorption path length versus sensitivity (dashed curve), the value of which is shown on the y axis (right). The red vertical line is the error bar representing the standard deviation. b) The path length is sorted according to the source-detector separation.

The error-bar value is small compared to the corresponding oxygen absorption path

length, which means that the light propagation in such a model is stable. In figure 26a, a high sensitivity value does not indicate a long oxygen absorption path length. This could be understood from the definition of sensitivity, because it is only representing the fraction of the absorption path length in the lung to the total light propagation distance. For example, a low sensitivity may indicate a low fraction of absorption path length in the lung but its absolute value could be larger than that with a higher sensitivity value. Another important reason is that in the simulation, the lung region is assigned to the optical properties of $\mu_a = 0$ cm^{-1} and $\mu_s' = 10$ cm^{-1}. While in the physical model, the lung is air-filled and the scattering is caused by the nylon boundary, a highly scattering material with $\mu_s' = 43.8$ cm^{-1}. So a deviation between measured absorption path length and sensitivity values is expected but the relation is unclear. For figure 26b, there is also no sign indicating that the oxygen absorption path length is proportional to the source-detector separation.

The water vapour absorption path length is plotted together with its corresponding oxygen absorption path length in figure 27. The error for the water vapour path length is also small. From observation, the trend of the oxygen and water vapour absorption path length is similar, and therefore the assumption is fulfilled that we can use the measured water vapour absorption path length to replace that of oxygen, and thus the oxygen concentration can be calculated.

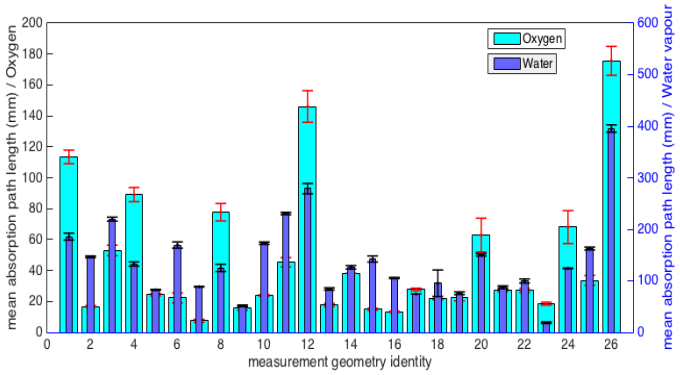

Figure 27: In this figure, the y axis (left)represents the path length values for oxygen signal, from limits of 0 mm to 200 mm. The y axis (right) is for the water vapour, from limits of 0 mm to 600 mm.

However, when comparing the absolute values of the water vapour and oxygen absorption path length (figure 27) it shows that the 935 nm laser probes a much longer path length in the lung than the 760 nm. Here we make the assumption that the water vapour concentration in the lung is the same as in the air, which is 1.02% as calculated in section 2.8.8. In fact, the water vapour concentration in the lung could be higher. Because when doing ventilation to the lung with dry nitrogen, the nitrogen becomes wet when it comes out from the lung, which means that some water vapour is flushed out. This could be that a certain amount of the muscle liquid diffuses into the lung

continuously, producing water vapour all the time. The liquid diffusion is very small because we found no sedimentation of liquid in the lung when the measurements were finished. Therefore, although the temperature is the same both in the lung and air, the relative humidity in the lung could be much higher than 32.5% of that in air, and it will lead to a calculation of shorter absorption path lengths.

To quantitatively investigate the relation between the water vapour and the oxygen absorption path length, a simple linear regression method is utilised to describe the correlation between the water vapour and the oxygen absorption path length. Before implementation, we should first examine the Levenberg Marquardt non-linear fitting of the reference signal to the sample signal.

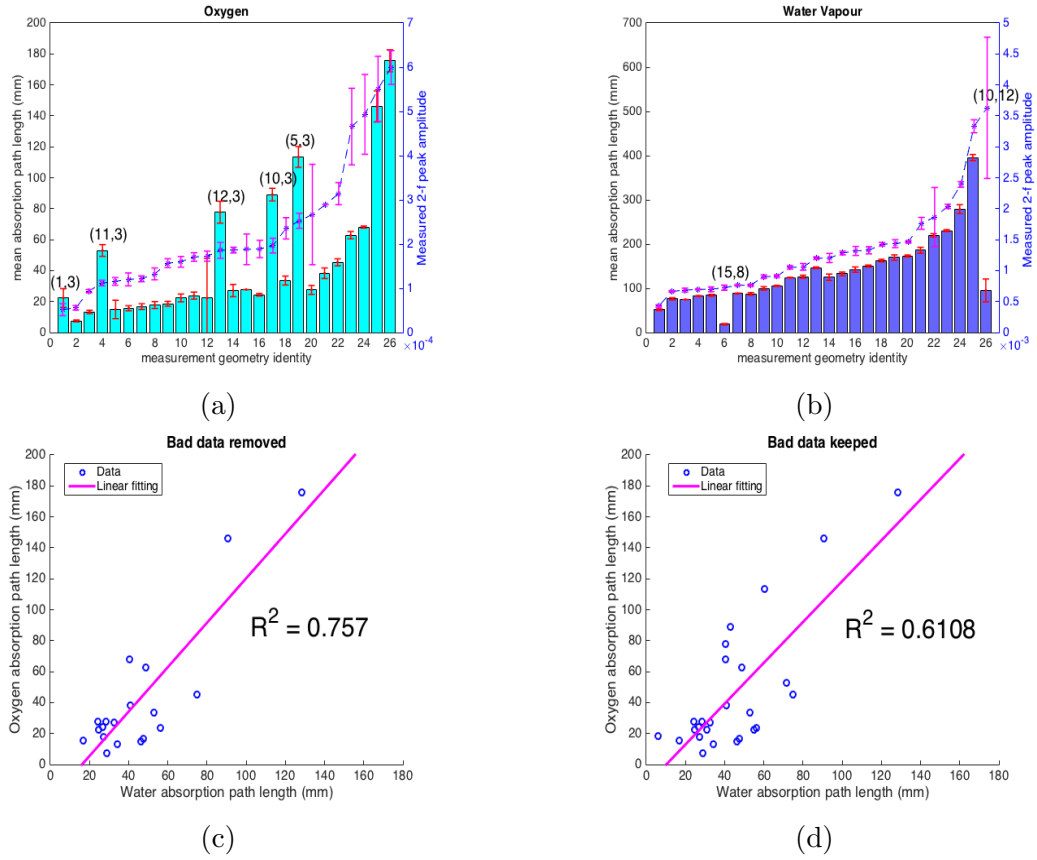

Figure 28: a) The oxygen absorption path length, along with its corresponding measured peak amplitude of $2f$ signal, the value of which is shown on the y axis (right). b) The case for water vapour. c) The linear regression plot where the water vapour absorption path length is at x axis (bottom), oxygen at y axis (left). The bad data is removed and the R square value is 0.7457. d) The linear regression with the bad data kept, and the R square as 0.6108.

In figure 28a, the oxygen absorption path length is plotted along with its corresponding measured peak value of the $2f$ signal. Overall, the absorption path length increases as

the measured $2f$ signal peak increases, which means that the non-linear fitting behaves correctly. But it is not accurate for all the measurement geometries (source,detector), some data points have a miss match of their path length values and their associated 2f peak values (figure 28b). The bad fitting results from a signal with a very low SNR, where interference fringes disturb the fitting procedure. The same procedure is also applied to the water vapour signal where in contrast the bar plot of absorption path length matches the curve of the $2f$ signal peak value very well, except for the two measurement geometries $(15, 8)$ and $(10, 12)$.

If the bad data are now removed, this enables us to do a better linear regression. The R^2 is calculated as 0.757 when the bad data is discarded, which indicates a good linearity (the closer for R^2 to 1, the better the prediction). Without discarding any data, the R^2 is 0.6108.

4.4.3 Nitrogen vs air

Figure 29 shows how the absorption path lengths for water vapour and oxygen change when the lung is flushed with dry and pure (100%) nitrogen.

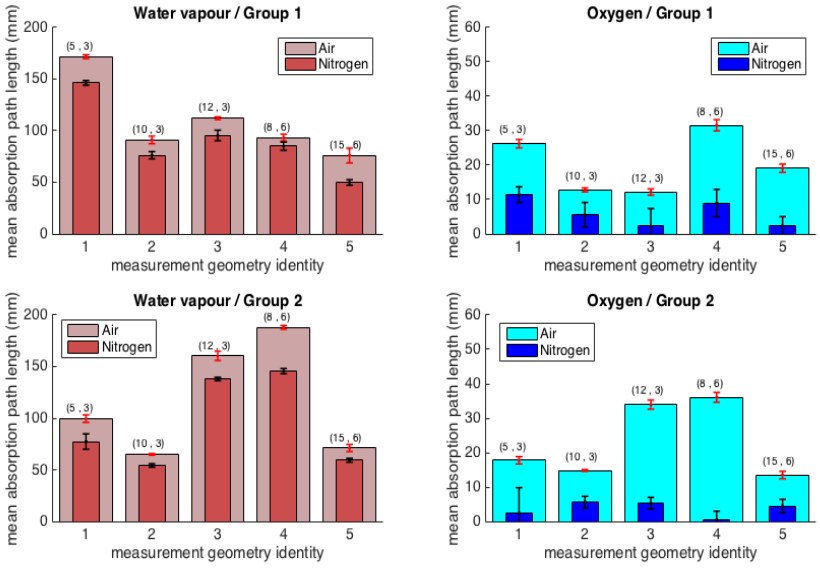

Figure 29: The bar plots on the top row show the absorption path length for water vapour and oxygen respectively in group 1 measurement under atmosphere or nitrogen-flushed condition (see the legend); the number in parenthesis indicates the measurement geometry (source,detector). The bottom row are the results from group 2.

Although group 1 and group 2 are two identical measurements (group 2 is the repetition of group 1), the calculated absorption path lengths for the water vapour or the oxygen

at the same measurement geometry, like at (source,detector) of $(5, 3)$, can be different. This discrepancy could be caused by the slightly different optical properties of the liquid phantoms of group 1 and group 2. What does not change in group 1 and group 2 is the fact that even though the lung is flushed with pure nitrogen, the water vapour laser still probes a long absorption path length in the lung. Recall the discussion for figure 27 about the observation that some water vapour is blown out from the lung when it is flushed with dry nitrogen, so if we take this fact into account, the result in figure 29 is understandable. Because the water vapour concentration is maintained for the continuously diffusion of liquid through the lung wall. For the oxygen signal in group 1 and group 2, there is a significant decrease in the probed absorption path length when the lung is nitrogen-flushed. The error-bars when flushing with nitrogen are comparative to their corresponding calculated absorption path length, and this implies that the SNR is low and the fitting of the raw $2f$ oxygen signal is heavily influenced by the noise and interference fringes. Therefore, the calculated absorption path length under nitrogen-flushing conditions may not really come from the oxygen absorption, it could be the fitting to the noise or fringes.

If the decrease of water vapour absorption path length is caused by the water vapour that is transported out when flushing nitrogen through the lung, then for a slow enough nitrogen flow to not carry too much water vapour out at a time, we could expect that the absorption path length stays constant no matter inside the lung is air or pure nitrogen. In order to verify the assumption, the water vapour detection is recorded continuously from flushing the lung to stop flushing with nitrogen (figure 30). At the same time, the oxygen is also recorded to make sure the lung is 100% full of nitrogen, indicated by zero absorption path length. The measurement is done on one random measurement geometry.

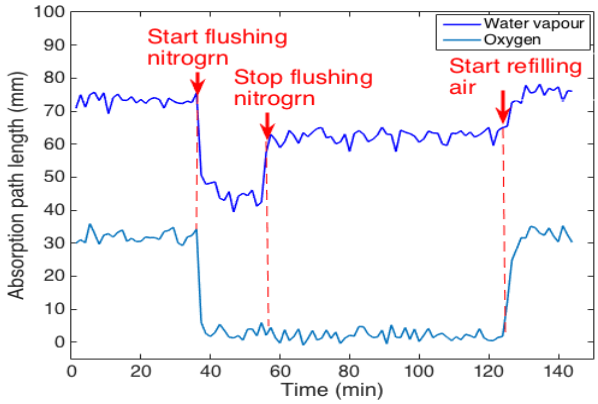

Figure 30: The record of the absorption signal for both water vapour and oxygen starts when the lung is air-filled. After that the lung is nitrogen-flushed and continuously for 30 minutes. The flush is stop and the record is still undergoing. The lung is refilled with air again.

Before flushing nitrogen, the probed absorption path length for water vapour is 72 mm,

and 30 mm for oxygen. When flushing with nitrogen, both absorption signals drop down immediately and there is no oxygen in the lung (indicated by the zero mm absorption path length), while there is still a certain amount of water vapour (45 mm). This is expected because it is the same case as shown in figure 29. When the flushing stops (the lung is still full of nitrogen afterward), the water vapour signal increases immediately. To a certain extent, this explains the assumption that the water vapour is not being transported out by the flushing of nitrogen, the concentration increases. The difference is that it does not increase back to the normal situation when the absorption path length is 72 mm, instead it increases to another lower absorption strength, 60 mm, and is stable for a long time. A possible reason could be that the nitrogen is cold, which changes the temperature in the lung. Therefore the water vapour concentration is lower than normal and it may take more than an hour for the temperature to increase to room temperature. What can be done to further confirm the assumption is to repeat the measurement at a much higher flow rate, we could expect the absorption signal to decrease to lower than 45 mm during flushing and increase back to the same 60 mm when the flushing ends. A thermometer can be used to monitor the temperature in the lung.

Considering the offset of the oxygen absorption signal observed in figure 29, a possible contribution could originate from bubbles in the liquid phantom. Therefore, GASMAS measurements on the liquid phantoms are also implemented. Figure 31 shows the mean $2f$ signal, averaged by 40 seconds, of water vapour and oxygen for the liquid phantoms simulating the fat and muscle tissue. As it can be observed, all absorptions signals of water vapour and oxygen are strongly affected by noise. Therefore, we can conclude that there are no bubbles in the liquid phantoms. From the set up shown in figure 16, the source and detector separation is 75 mm. While in the model, between the outermost surface and the boundary of the lung there is a short distance starting from a fat layer about $4 \sim 8$ mm, followed by a muscle layer about $3 \sim 6$ mm. Even though there are bubbles made by mistake when preparing phantoms, the caused absorption signal offset is still negligible.

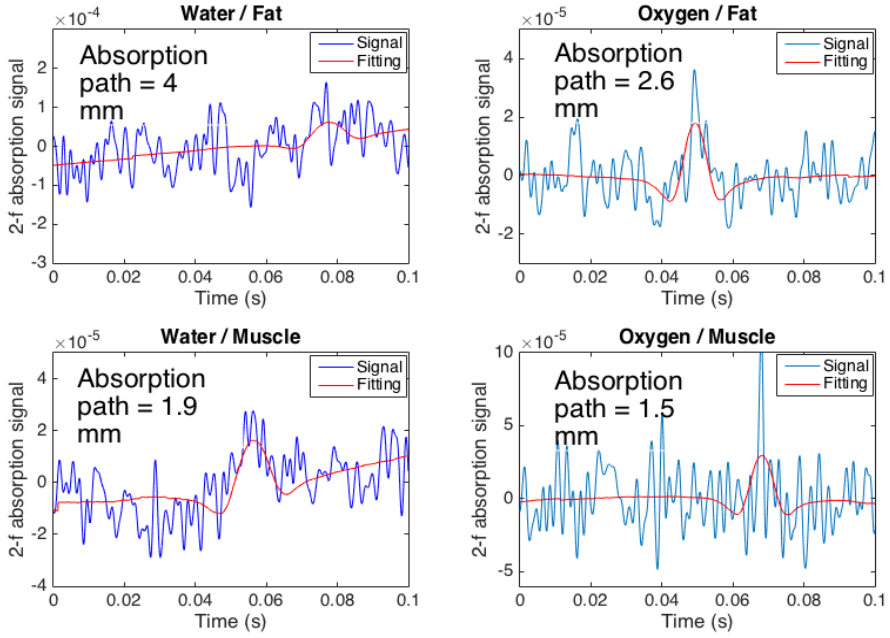

Figure 31: The top row shows the raw $2f$ signal and its fitting curve of water vapour and oxygen for the fat liquid phantom and the text in each graph tells its calculated absorption path length; the bottom row shows the result for muscle liquid phantom; see the titles and the legends.

5 Summary and Outlook

In this thesis work, a robust 3D plastic model with a similar body structure to a newly born infant is successfully constructed and printed. The geometry totally depends on the segmentation of the raw CT images, which is an artificial manipulation. There are undoubtedly some mismatch of the shape of the tissues between the segmentation and its raw images. Especially for the skin which has a thickness below 1 mm for the infants, it is difficult to segment exactly the same size as that shown in the CT. As a result, a significant manual contribution to the tissue segmentation is done in order to ensure the precision. Six tissue types are segmented in Nirfast and only four of them are printed using nylon. The bone is printed in solid because the structure is too complex to be printed hollow. The skin layer in not able to be printed because of its thin thickness. The lung, heart and fat are printed hollow with a wall thickness of 0.5 mm, 0.5 mm and 0.7 mm respectively. Although the nylon surface of these printed models may not affect the light absorption because $\mu_{a,nylon} = 0.023$ cm^{-1} is very low, the high scattering coefficient of nylon affect the light scattering significantly. This was observed by that the signal was improved a lot if the wall thickness of the fat model decreased by 0.1 mm. However, a certain wall thickness has to be applied to guarantee no leakage of the liquid phantom through the fat tissue model layer. One potential way

to decrease the 0.7 mm wall thickness by 0.1 or 0.2 mm is to smooth the surface of the model. The CT slices are taken every 0.7 mm in the z axis, while the accuracy of the printing is 0.1 mm per slice. So either we acquire a CT series with higher resolution, or some smoothing image technique should be applied to produce a smooth gradient of change between two consecutive segmented images.

The optical properties at 760 nm of these six tissues are determined by comparing and combining the literature data, and from the calculation of the four chromophores (water, fat, oxy- and de-oxy hemoglobin) with their associated concentrations. However, it is difficult to judge the reliability of the concluded optical properties. Because for each tissue, the found literature data vary a lot because the measurements were done on different samples; while for the chromophore assumption, there is an uncertainty in the concentration of the different chromophores, especially when considering the target is a preterm infant who has immature tissues. However, we conclude that the optical properties are reasonable. Since the GASMAS measurements are implemented based on the simulation results, it is more crucial to make the optical properties the same as that in the simulation when preparing the liquid phantoms.

From the simulation results, the fraction of the light propagation distance in the lung, defined as the sensitivity, depends on the position of the sources and the detectors. It is not determined by the source-detector separation or the power of incident light. This result may indicates that when doing practical GASMAS measurements on the infants in clinical trial, the source and the detector may need to be moved around the lung until a strong absorption signal of oxygen is found. GASMAS measurements are performed on those suggested source-detector geometries, selected by a detectable intensity and a high sensitivity, from the simulation results. However, there are no similarity between the probed absorption path length from the GASMAS measurements and the sensitivity obtained from the simulation. The main reason probably is that the 3D printed model has the nylon surface which is absent in the simulation. More repetition on the GASMAS measurements should be done to further statistically analyse the relationship between the probed absorption path length from the 3D model and the sensitivity values obtained from the simulation.

Another important investigation is to examine the validity of the assumption that the water vapour absorption path length probed by 935 nm is equivalent to that of 760 nm. A linear relationship is obtained with $R^2 = 0.7574$ after removing bad fitting data. But their amplitudes are not of the same order, with around a difference of a factor 3. When calculating the absorption path length for water vapour by using the reference signal, perhaps we can not assume that the water vapour concentration in the lung is the same as in the air. From the nitrogen flushing measurements, there is still water vapour even though the lung is full of pure nitrogen. The water vapour may come from the continuously diffused liquid from the muscle to the lung because the wall thickness is just 0.5 mm. Therefore, it is more reasonable to believe that the water vapour is

abundant in the lung and more possible that the water vapour concentration is higher than in air. Measurements to determine the true values of the relative humidity and the temperature in the lung are required in order to calculate the water vapour absorption path length accurately.

In conclusion, oxygen detection in the lungs is successful in the 3D printed infant model, as long as the laser power is sufficiently high and the detector is sensitive enough. In later stage of the project, the 935 nm laser would be replaced by a laser lasing at 820 nm, which is closer to the absorption of oxygen at 760 nm, in order to have more similar light propagation behavior. The 3D model can be further improved by adding the skin layer, and the lung should be made more complex with not just air inside. The wall thickness of the model should also be decreased. If possible a better printing material instead of nylon should be investigated in order to reduce its influence on the light propagation.

References

[1] Emile Krite Svanberg, P. L. "Diode laser spectroscopy for noninvasive monitoring of oxygen in the lungs of newborn infants." Doi:10.1038/pr.2015.267

[2] S. A. Sullivan, O. S. A. J. (1963). "Experimental study of the absorption in distilled water, artificial sea water, and heavy water in the visible region ofthe spectrum." 53, 962–968.

[3] R.L.P. van Veen and H.J.C.M. Sterenborg, A. P., A. Torricelli and R. Cubeddu. "Determination of VIS- NIR absorption coefficients of mammalian fat, with time- and spatially resolved diffuse reflectance and transmission spectroscopy." OCIS codes: 160.4760.

[4] Tomas Svensson, S. A.-E. "Laboratory manual: Time resolved spectroscopy." Department of Physics, Lund University.

[5] Hayat, M. A. "Cancer Imaging: Lung and Breast Carcinomas." Page: 446.

[6] Weiss, O. K. D. a. G. H. (2005). "Photon Diffusion in Biological Tissues." Diffusion Fundamentals 2 (114.1 - 114.21).

[7] Yodh, A. G. "Diffuse Optics: Fundamentals Tissue Applications." Department of Physics Astronomy University of Pennsylvania.

[8] Micheal S.Patterson, S. J. M. (1991). "Diffusion equation representation of photon migration in tissue." IEEE.

[9] Tomas Svensson, C. A. (March 23, 2011). "Time Resolved Spectroscopy,Laboratory Exercise." Department of Physics, Lund University.

[10] Michael Wahl,PicoQuant GmbH, Rudower Chaussee, (2014). "Time-Correlated Single Photon Counting." PicoQuant Gmbh, Germany.

[11] David A.Boas, C. P., Nimmi Ramanujam. "Handbook of biomedical optics, Chapter 5."

[12] URL: http://www.ucl.ac.uk/medphys/research/borl/intro/skin

[13] Hall, G. a. "Textbook of Medical Physiology, the tenth edition." chapeter 32, page 382.

[14] "Blood" Wikipedia. URL: https://en.wikipedia.org/wiki/Blood.

[15] Hans van Assen, P. B., Tammo Delhaas "Functional Imaging and Modeling of the Heart: 8th International Conference".

[16] Marleen Keijzer, R. R. R.-K., Steven L. Jacques, and Michael S. Feld. "Fluorescence spectroscopy of turbid medium: Autofluorescence of the human aorta." Doi: 10.1364/AO.28.004286

[17] Patrik Lundin, M. L. (May 11 2010). "Medical Optics Project."

[18] Stefan Andersson-Engels, T. S., Johan Axelsson (February 19, 2015.). "Photon Diffusion; Computer Exercise." Department of Physics, Lund University.

[19] Steven L Jacques. (26 February 2013). "Optical properties of biological tissues: a review." Institute of Physics and Engineering in Medicine.

[20] H. H. MITCHELL, T. S. H., Ii. R. STEGGERDA, AND H. W. BEAN (February 15, 1945). "The chemical composition of the adult human body and its bearing of the biochemistry of growth."

[21] THOMAS, L. W. (4th January 1962). "THE CHEMICAL COMPOSITION OF ADIPOSE TISSUE OF MAN AND MICE." the Department of Physiology, Edinburgh University.

[22] Ann L. Albright , J. S. S. "ADIPOSE TISSUE." Department of Nutrition and Internal Medicine,University of California at Davis.

[23] Lorenzo Spinelli, F. M. (28 May 2007). "Calibration of scattering and absorption properties of a liquid diffusive medium at NIR wavelengths. Time-resolved method." OPTICS EXPRESS 6589. Vol.15 No. 11 /

[24] Paola Di Ninni, F. M., and G.Zaccanti "The use of India ink in tissue-simulating phanto." Doi:10.1364/OE.18.026854

[25] Rene Michels, F. F., an dA . Kienle.1 (4 April 2008). "Optical properties of fat emulsions (orange dash line in Fig.11.)" OPTICS EXPRESS 5907. Vol.16, No.8

[26] Svensson, T. "Pharmaceutical and Biomedical Applications of Spectroscopy in the Photon Migration Regime." Lund Reports on Atomic Physics, LRAP-392. ISSN:0281-2762

[27] Pawel Kluczynski, O. A. "Theoretical description based on Fourier analysis of wavelength-modulation spectrometry in terms of analytical and background signals."

[28] Liang Mei, S. S. "Wavelength modulation spectroscopy—digital detection of gas absorption harmonics based on Fourier analysis." Doi: 10.1364/AO.54.002234

[29] B.E.A. Saleh, M. C. T. "Fundamentals of photonics, second edition." A John Wiley Sonc, Inc., Publication

[30] McRae, G. J. "A Simple Procedure for Calculating Atmospheric Water Vapor Concentration." Air Pollution Control Association. DOI: 10.1080/00022470.1980.10464362

[31] M. Jermyn, H. G., M.A. Mastanduno, W. Turner, S.C. Davis, H. Dehghani, and B.W. Pogue,J. Biomed (12 Augus, 2013). "Fast segmentation and high-quality three-dimensional volume mesh creation from medical images for diffuse optical tomography." Opt. 18 (8), 086007. Doi: 10.1117/1.JBO.18.8.086007

[32] H. Dehghani, M. E. E., P.K. Yalavarthy, S.C. Davis, S. Srinivasan, C.M. Carpenter, B.W. Pogue, and K.D. Paulsen "Near infrared optical tomography using NIRFAST: Algorithm for numerical model and image reconstruction." Vol. 25, 711-732 (2009)

[33] Bathe, K.-J. (2008). "Finite Element Method." Wiley Encyclopedia of Computer Science and Engineering. 1–12.

[34] Suliga M, D. R., Nyssen E "Markov random field-based clustering applied to the segmentation of masses in digital mammograms." Doi:10.1016/j.

[35] URL: http://www.mathworks.com/matlabcentral/fileexchange/20922-stlwrite-filename–varargin-

6 Appendix.A - Printed tissue models

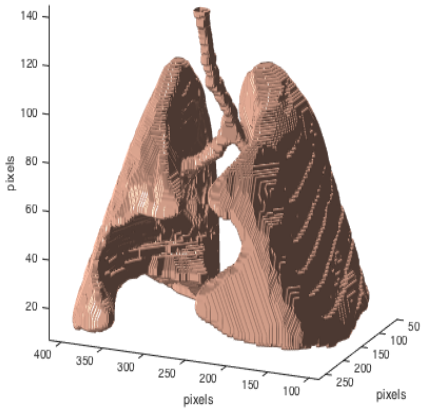

(a) lung in Matlab

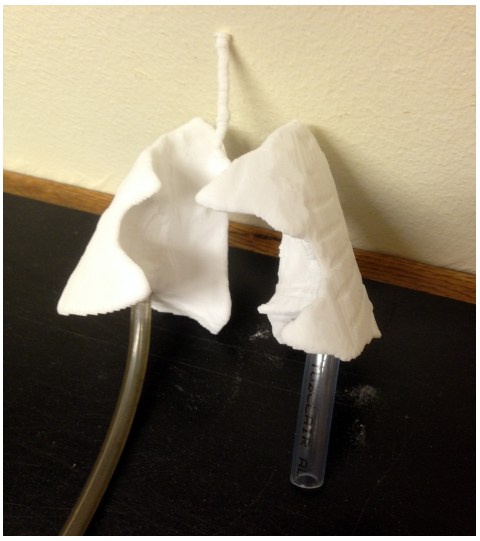

(b) lung printed

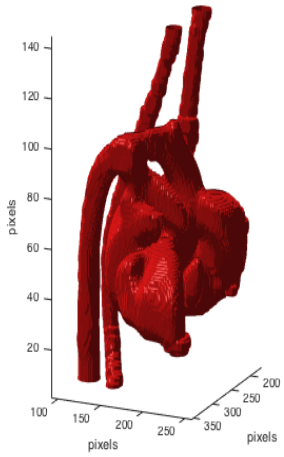

(c) heart in Matlab

(d) heart printed

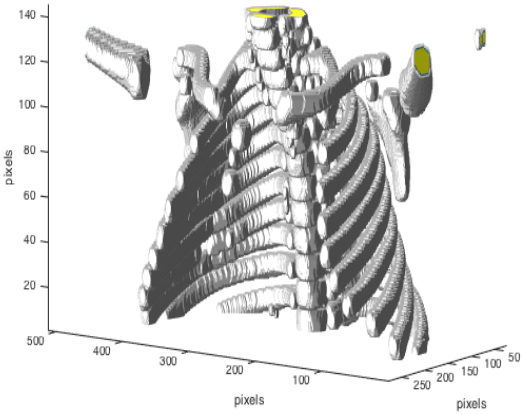

(e) bone in Matlab

(f) bone printed

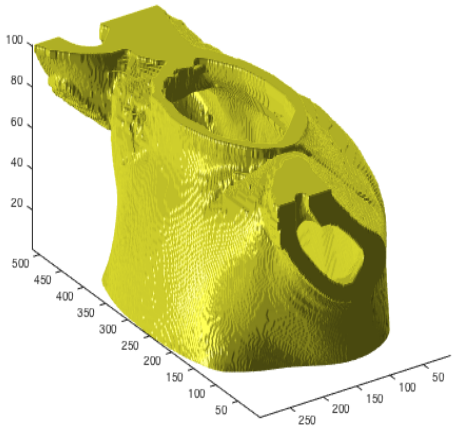

(g) fat in Matlab

(h) fat printed

7 Appendix.B - calculation of predicted optical properties at correct wavelengths from literature

Absorption properties extraction at interested wavelength, the **absorption spectra** mat data is provided by the lab exercise [18]

```
function [result,new_mua] = concentration_extract(a,b,varargin
    )
% a for the 1xn array of the wavelength
% b for the nx1 array corresponding absorption coeff in cm-1
% till example: a = [700 800 900 1000];
%               b = [1.1100;1.0700;1.0700;1.060];
%               c = [725 760 820 935];
%               [result new_result] = concentration_extract(a,
    b,'skin',c);

load absorption_spectra
n = length(a);
A = cell(1,n);
B = cell(n,4);

for i = 1:n
A{1,i} = find(data.wavelength == a(i));
B{i,1} = data.hb(A{1,i});
B{i,2} = data.hbo2(A{1,i});
B{i,3} = data.lipid(A{1,i});
B{i,4} = data.water(A{1,i});
end

BB = cell2mat(B);
% disp(BB);
tissue = cell(2,4);
[tissue{1,:}] = deal('C_hb','C_hbo2','C_lipid','C_water');

text = varargin{1};
disp(['the tissue you have enter is: ' text])
tissue_name = {'skin','fat','muscle','lung','heart','bone'};
pos = strcmp(text,tissue_name(1:6));
index = find(pos,1);
switch index
    case  1
        result = BB\(b.*100);
```

```
35          [tissue{2,:}] = deal(result(1),result(2),result(3),
                result(4));
36          sprintf('%s: %4f\n',tissue{:})
37      case  2
38          result = BB\(b.*100);
39          [tissue{2,:}] = deal(result(1),result(2),result(3),
                result(4));
40          sprintf('%s: %4f\n',tissue{:})
41      case  3
42          % mua = c_myoglobin*mua(lambda) + c_heamglobin*mua(
                lambda);
43          % c_myoglobin ~= c_heamglobin
44          sum1 = 0;
45          sum2 = 0;
46          for k = 1:n-1
47          group = cell(1:5);
48          group{k} = BB(k:k+1,1:2)\(b(k:k+1).*100);
49          sum1 = sum1 + group{k}(1);
50          sum2 = sum2 + group{k}(2);
51          end
52          result = [sum1 sum2]./k
53      case  4
54          result = BB\(b.*100)
55      case  5
56          result = BB\(b.*100)
57      case  6
58          result = BB\(b.*100)
59  end
60
61          c = varargin{2};
62          y = @givenWavlength;
63          new_mua = y(c,result);
64          D = cell(2,4);
65          [D{1,:}] = deal(c(1),c(3),c(3),c(4));
66          [D{2,:}] = deal(new_mua(1),new_mua(2),new_mua(3),
                new_mua(4));
67          new_absorption_coeff = sprintf('%dnm: %4f\n',D{:})
68  end
```

```
1  function New_mua = givenWavlength(lambda,concentration)
2  load absorption_spectra
3  n = length(lambda);
4  A = cell(1,n);
```

```
5  B = cell(n,4);
6
7  for i = 1:n
8  A{1,i} = find(data.wavelength == lambda(i));
9  B{i,1} = data.hb(A{1,i});
10 B{i,2} = data.hbo2(A{1,i});
11 B{i,3} = data.lipid(A{1,i});
12 B{i,4} = data.water(A{1,i});
13 end
14 BB = cell2mat(B);
15 New_mua = BB*concentration./100;
16 end
```

8 Appendix.C - WMS signal phase adjusting and intensity normalisation

For phase adjusting after the harmonic signal extraction from a super Gaussian window, a phase-amplitude plot is introduced where the the real part of $S^*_{nf,filt}(t)$ is plotted on one axis and the imaginary part is plotted on the other axis. The amplitude of the signal is then represented by the distance from the plot to the origin and the phase is represented by the angle to the axis of real part. As to the first harmonic absorption signal, there is an offset from the origin, see figure 33a, which is caused by the fact that when the laser injection current is tuned, not only is the wavelength tuned, but also the output intensity is modulated, which is called the Residual Amplitude Modulation (RAM). See the triangular shape of detected intensity in figure 9. As a result, there is a phase shift between the intensity modulation and the frequency modulation, which is the difference between alpha 1, the phase of RAM, and beta 1, the phase of $1f$ signal. The phase of $1f$ signal is the same as that of frequency modulation. While for $2f$ signal, there is no offset.

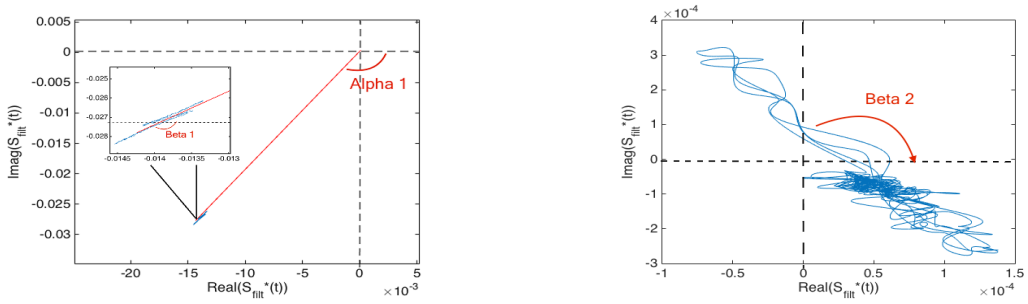

(a) (b)

Figure 33: a) and b) show respectively the phase plot of the first and second harmonic resulted from a measurement on the 3D printed model with liquid phantom with $\mu'_s = 10$ cm^{-1} filled in. The gas absorption signal comes from the water vapour in the lung. For the 1f signal, there is the offset from the origin, and the alpha 1 and beta 1 corresponds to the phase of RAM and the phase of absorption-related 1f signal, respectively; while the 2f signal goes through the origin and there is only beta 2.

The real WMS signal can then be achieved if the phase is adjusted for the harmonic signal, and the offset (only needed for 1f signal). See the equation:

$$S_{nf,filt}(t) = Re\left\{S_{nf,filt} * (t) - mean(S_{nf,filt} * (t)) \times exp(-i \cdot beta_{nf})\right\} \ , \qquad (19)$$

Further, in order to get the signal amplitude that is directly proportional to the absorbance of the gas, the real WMS signal $S_{nf,filt}(t)$ is intensity-normalised with the triangular shape scanning intensity (frequency of 5 Hz), which is the RAM. A polynomial fitting is applied to the up and down slope of two sides of the detected intensity profile separately, and the normalisation is done by dividing $S_{nf,filt}(t)$ by the fitting

result. A first degree polynomial is sufficient to describe the RAM because usually the output power from a laser diode is linear to the injection current. See the equation below:

$$\overline{S}_{nf,filt}(t) = \frac{S_{nf,filt}(t)}{p_0 + p_1(t)} \ , \tag{20}$$

where p_0 and p_1 are the parameters of the fitted curve. However, to avoid the non-linearity effect from the gas absorption (see the dip in figure 9c), the sample points that are away from the absorption dip, shown in figure 34, are used to do polynomial fit. For example, the fitted slope of left side is determined by the mean of the data points (x axis) in that two selected parts and the mean of their corresponding values (y axis).

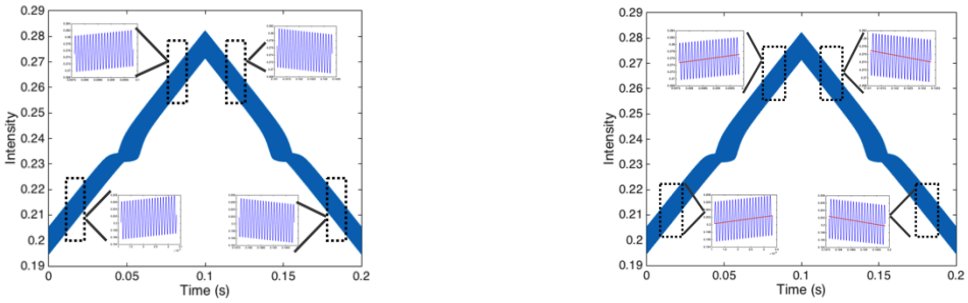

(a) (b)

Figure 34: a) The four selected part of the detected signal used to do the fitting to the slopes of the two side separately. b) The fitting result, indicated by the red line.